The Dissertation Committee for Xiang Hu
certifies that this is the approved version of the following dissertation:

Topological phases in thin films of pyrochlore iridates along the [111] direction

Committee:

Gregory A. Fiete, Supervisor

Zhen Yao

Qian Niu

Allan H. MacDonald

John B. Goodenough

Topological phases in thin films of pyrochlore iridates along the [111] direction

by

Xiang Hu, B.E.;M.S.;M.S.

DISSERTATION

Presented to the Faculty of the Graduate School of

The University of Texas at Austin

in Partial Fulfillment

of the Requirements

for the Degree of

DOCTOR OF PHILOSOPHY

THE UNIVERSITY OF TEXAS AT AUSTIN

August 2015

Dedicated to my parents.

Acknowledgments

Six years ago, my passion for science led me to Austin, a place where I can incubate my dreams. Six years later, when I reflect on my experience, I would like to thank my advisor, Dr. Greg Fiete especially. He is the nicest and most helpful advisor who is willing to help me in any aspect. Dr. Fiete is willing to help me solve any problem, no matter if it is about physical insights, or detailed technical problems, or just philosophical thinking, or everyday issues. When I was seeking a postdoctoral position, he even helped me revise my research statement and curriculum vitae. Dr. Fiete always listens to my opinions carefully, and fully understands my situation. When I was in a low mood, he always encouraged me. When I got stuck in my research, he always tolerated my slow progress. Instead of emphasizing publications, Dr. Fiete revealed to me what is the persistent pursuit of truth, the most valuable spirit of a real scientist.

Sincere thanks to my committee members Dr. John Goodenough, Allan MacDonald, Yao Zhen and Qian Niu, who spent their valuable time helping me throughout my whole program and final dissertation. Thanks to all my teachers at the University of Texas (UT), who opened new windows of knowledge in front of me.

Thanks to Greg Fiete, Allan MacDonald and Chin-Sen Ting for your

recommendations in support of my postdoctoral applications.

I appreciate my dear collaborators Zhicheng Zhong, Craig Fennie, Priyamvada Jadaun, Mehdi Kargarian, Penghao Xiao, Chandrima Mitra, Andreas Rüegg, Qi Chen, Hsiang-Hsuan Hung, Hongbin Zhang, Xiaoran Liu, and Jacques Chakhalian. Without the support from you, it would have been impossible for me to finish my degree study.

I need to thank my roommates Dejun Li, Zhongyu Yuan, Jianyong Mo, Yihan Huang, Yu Chen, and Yi-Der Lin. I always remember those days we spent together, tasting delicious foods, watching basketball games, and sharing everyday experiences. I miss the days I played badminton with Yang Gao, Libin Zhang, Rongting Zhang, Roger Li, and other friends. Your friendship helps to relieve my homesickness, and make Austin a wonderful place.

I want to express my gratitude toward other group members Liang Du, Xiaoting Hao, Pontus Laurell, Rex Lundgren, Jun Wen, Georgios Stamokostas, Stewart Koppell, Victor Chua, Seth Whitsitt, and Vladimir A. Zyuzin. I enjoy the warm and encouraging atmosphere in this group. In addition, discussions with you always inspire me a lot. I appreciate Hua Chen, Zhenhua Qiao, Jian-Xin Zhu, Yingyue Lee, Yuan-Yen Tai, Donna Sheng, Hai-En Tsai, Wei Zhu, Shoushu Gong, and other teachers and colleagues for the generous help.

I also need to express my gratitude to the wonderful secretary Michele Landfield, my dear health providers, and my friends at UT Badminton Club and UT Science Toastmasters.

I appreciate all the people who have helped me.

Finally, I need to thank Sue Leung, my parents, and the whole family of my sister. Your encouragement and constant support is the most important driving force for my research.

Topological phases in thin films of pyrochlore iridates along the [111] direction

Publication No. _____

Xiang Hu, Ph.D.
The University of Texas at Austin, 2015

Supervisor: Gregory A. Fiete

Topological states in (quasi) two-dimensional systems have attracted a lot of attention, both theoretically and experimentally, since the discovery of quantum Hall effect. In this thesis, we first introduce the ruby lattice which is able to host an extremely flat topologically non-trivial band. This helps to realize integer and fractional quantum Hall effect in lattices. We then study the thin films of pyrochlore iridates grown along the [111] direction. We first investigate a semi-empirical model described by a multi-band Hubbard model. Using Hartree-Fock approximation, our phase diagrams predict that the bilayer and triangular-Kagome-triangular trilayer structures are the most favorable for topological phases. We then check those structures with first-principles calculations, and find they are able to support the Z_2 topological metallic phase and Chern metallic phase. We study in detail the extended

nature of $5d$ orbitals. As a consequence, the charge-density wave caused by nearest-neighbor interaction may serve as a possible way to turn these topological metallic phases into their insulating counterparts.

Contents

Chapter 3. Thin films of pyrochlore iridates: a semi-empirical model 28

List of Tables

List of Figures

Chapter 1

Introduction

1.1 Quantum spin Hall effect and quantum anomalous Hall effect

More than one hundred years ago, when the young Edwin Herbert Hall[1] was reading Maxwell's *A Treatise on Electricity and Magnetism (Vol.2)*, he was puzzled by one statement:

"It must be carefully remembered, that the mechanical force which urges a conductor carrying a current across the lines of magnetic force, acts, not on the electric current, but on the conductor whiclh carries it."

He began to question that statement. No one would likely to anticipate that one hundred years later, Hall's questioning will bring a storm to the community of physics.

In 1980[2] and 1983[3], the studies of two-dimensional electron gases led to the discovery of the integer and fraction quantum Hall effects (QHE). In those phenomena, the Hall conductivity is quantized as

$$\sigma_{xy} = \nu \frac{e^2}{h}.$$ (1.1)

Here ν is an integer or fractional number.

Using Kubo's formula and the TKNN[4] formula, one can confirm that for the integer QHE, the quantization number satisfies

$$n = \frac{1}{2\pi} \int d^2 \mathbf{k} \mathcal{F}, \tag{1.2}$$

where $\mathcal{F} = \nabla \times \mathbf{A}$ is the Berry curvature, and $\mathbf{A}$ is the Berry connection.

This relationship reveals some fundamental aspects of the ground state of quantum Hall systems. Unlike the states in Landau's second order phase transition theory, these phases are not classified by their symmetries, but by their intrinsic topological properties. The topologically different quantum Hall state and vaccum state are separated by edge states at the boundary. When the electron flows through the edge, the resistivty is zero since no back scattering occurs. However, this dissipationless currents can not be used in the real electronic systems, because the realization of the quantum Hall effect requires very strong magnetic fields and very low temperatures.

In 1988, Duncane Haldane[5] proposed a model residing on a honeycomb lattice. With the periodic magnetic flux across the lattice, it is possible to realize the quantum Hall effect without the external magnetic field.

Haldane's model is given by:

$$
\begin{aligned}
H(\mathbf{k}) \;=\;& 2t_2 \cos\phi \left(\sum_i \cos(\mathbf{k} \cdot \mathbf{b}_i) \right) I + t_1 \left(\sum_i [\cos(\mathbf{k} \cdot \mathbf{a}_i)\sigma^1 + \right. \\
& \left. \sin(\mathbf{k} \cdot \mathbf{a}_i)\sigma^2] \right) + \left[M - 2t_2 \sin\phi \left(\sum_i \sin(\mathbf{k} \cdot \mathbf{b}_i) \right) \right] \sigma^3, \quad (1.3)
\end{aligned}
$$

where t_1 and t_2, ϕ , and M are some parameters. σ are the Pauli matrices. $\mathbf{a}$

and **b** are basis vectors. In the half-filling case, Haldane calculated the Chern number of the system, and found it was non-zero.

Haldane's model opened the way toward quantum anomalous Hall effect (QAHE), the quantum Hall effect without external magnetic fields. However, it is very hard to be realized.

In 2005, after the discovery of graphene[6], Kane and Mele constructed another model[7] like the following:

$$\mathcal{H} = \sum_{\langle ij \rangle \alpha} t c_{i\alpha}^\dagger c_{j\alpha} + \sum_{\langle\langle ij \rangle\rangle, \alpha\beta} i t_2 \nu_{ij} s_{\alpha\beta}^z c_{i\alpha}^\dagger c_{j\beta}. \tag{1.4}$$

In graphene, the Fermi surface crossed the Dirac points. Due to the sensitivity of the system to perturbations, even a small spin-orbit coupling can act as "effective magnetic fields" and gap out the system. For different spin species, the effective magnetic field takes opposite directions. Therefore, the Kane-Mele model can be regarded as two-spin copies of the Haldane model.

Through a stripe geometry calculation, they proved the system has robust edge modes, similar to the edge states in quantum Hall effects. The robust edge states originate from the topological difference between the k-space structure of the model and vaccum. Kane and Mele introduce a Z_2 topological number[8], which is be equal to $\mod ((C\uparrow - C\downarrow)/2, 2)$, to describe the difference between the topological state and normal trivial insulating state. The special phenomenon they discovered is called the quantum spin Hall effect (QSHE).

Although the Kane-Mele model was first introduced for graphene, the spin-orbit coupling strength in graphene is too weak to experimentally realize the QSHE. The QSHE was first realized in the CdTe/HgTe/CdTe quantum wells[9] composed of heavy elements.

The structure of the quantum well is the following: The HgTe film is sandwiched between CdTe substrates. The system can be described by a quasi two dimensional model with four bands. Compared to CdTe, bulk HgTe has inverted band structure due to much stronger spin-orbit coupling(SOC). In the quantum well, the experiment[9] proves that if the width of the HgTe layer is larger than a critical value, the band inversion in HgTe causes a topological insulating phase in the two dimensional electron gas inside the HgTe layer. In addition, the non-trivial edge states are further confirmed.

From that time on, other topological insulators such as Bi_2Se_3, Bi_2Te_3 [10–23] have been discovered.

The QSHE still preserves time reversal symmetry. If the system is magnetically dopped, it is possible to polarize the electrons to suppress one spin component, and obtain the single-spin copy of the Haldane model, that is, the QAHE[24].

In 2013, Dr. Xue's group finally observed the QAHE in Cr-doped $Bi_{2-x}Sb_xSe_3$[25].

1.2 Density functional theory and Wannier functions

1.2.1 A brief introduction to density functional theory

Density functional theory (DFT) is widely used in the study of solid materials. It is based on the Kohn-Sham equation[26]. Here we give a simple derivation of the Kohn-Sham equation.

For a many-body electron system with Coulumb interactions, the Hamiltonian can be writen as

$$H = \sum_i \left[-\frac{\hbar^2}{2m}\nabla_i^2 + V_{\text{ext}}(\mathbf{r}_i) \right] + \frac{e^2}{2} \sum_{i,j;i\neq j} \frac{1}{|\mathbf{r}_i - \mathbf{r}_j|}. \tag{1.5}$$

According to The Hohenberg-Kohn theorem[27], the total energy can be defined as a functional of the density:

$$E[n] = T[n] + \int \mathrm{d}^3 r n(\mathbf{r}) V_{\text{ext}}(\mathbf{r}) + \frac{e^2}{2} \int \mathrm{d}^3 r \int \mathrm{d}^3 r' n(\mathbf{r}') \frac{1}{|\mathbf{r} - \mathbf{r}'|} n(\mathbf{r}) + E_{\text{xc}}[n]. \tag{1.6}$$

Here $T[n]$ is the kinetic energy of the corresponding non-interacting case. All the many-body effects except the density-density interaction has been included in the exchange-correlation energy $E_{\text{xc}}[n]$.

Because the total electron number is fixed, after varying the density, one can obtain the minimum condition for the energy

$$\frac{\delta T[n]}{\delta n(\mathbf{r})} + V_{\text{xc}}[n] + \int \mathrm{d}^3 r' n(\mathbf{r}') \frac{1}{|\mathbf{r} - \mathbf{r}'|} + V_{\text{ext}}(\mathbf{r}) = \lambda, \tag{1.7}$$

where $V_{\text{xc}}[n](\mathbf{r}) = \frac{\delta E_{\text{xc}}[n]}{\delta n(\mathbf{r})}$ is the exchange-correlation potential.

Comparing this with the single particle problem, we can introduce an effective mean field,

$$V_{\text{eff}}[n] = V_{\text{ext}}(\mathbf{r}) + V_{\text{xc}}[n](\mathbf{r}) + \int \mathrm{d}^3 r' n(\mathbf{r}') \frac{1}{|\mathbf{r} - \mathbf{r}'|}. \qquad (1.8)$$

Then it is easy to write the corresponding Schrödinger equation

$$\left[\frac{\hbar^2}{2m} \nabla^2 + V_{\text{eff}}[n](\mathbf{r}) \right] \psi_i(\mathbf{r}) = \epsilon_i \psi_i(\mathbf{r}). \qquad (1.9)$$

The eigen wave functions should be consistent with the density by

$$n = \sum_{i=1}^{N} |\psi_i(\mathbf{r})|^2. \qquad (1.10)$$

This is the Kohn-Sham equation. It maps a many-body problem to a one-body problem by introducing the exchange-correlation potential. In principle, if one is able to learn the exact form of $V_{\text{xc}}[n]$, then the solution is exact. However, in practice, due to the complexity of the problem, one can only use approximations of $V_{\text{xc}}[n]$ such as the local density approximation (LDA) and the generalized gradient approximation (GGA).

1.2.2 Wannier functions

In crystals with translational symmetry, due to the commutation relation between the Hamiltonian and the translation operator, any translation operation on the energy eigenstates just creates a phase factor which depends on the wave vector and the basis vector. This is the origin of Bloch wave functions.

6

Bloch waves can be regarded as amplitude modulated plane waves, which are characterized by the envelop function $u_n(\mathbf{k})$ and the plane wave part $e^{i\mathbf{k}\cdot\mathbf{r}}$. If we can find a way for these Bloch waves to intervene with each other, it is possible to create wave packets localized at some sites. Mathematically, this is just a Fourier transformation from $\mathbf{k}$ space to real space

$$|\mathbf{R}n\rangle = \frac{V}{(2\pi)^D} \int_{\text{BZ}} d\mathbf{k} e^{-i\mathbf{k}\cdot\mathbf{R}}|\psi_{n\mathbf{k}}\rangle, \tag{1.11}$$

Here D is the dimensionality. These are called Wannier functions.

It is easy to verify the Wannier functions are orthonormalized, so they can be used as a basis for periodic systems. They are especially useful in the systems with localized electronic states, such as systems whose valence electrons are in $3d$ or f orbitals.

One of the basic properties of Wannier functions is nonuniqueness. For a given set of Bloch wavefunctions, one can define a local gauge field, and the Wannier functions become

$$|\mathbf{R}n\rangle = \frac{V}{(2\pi)^D} \int_{\text{BZ}} d\mathbf{k} e^{-i\mathbf{k}\cdot\mathbf{R}}|\sum_{m=1}^{J} U_{mn}^{(\mathbf{k})}\psi_{m\mathbf{k}}\rangle. \tag{1.12}$$

Here U is a set of unitary transformations corresponding to the gauge field.

Wannier functions have been proposed for many years. However, it was not widely used in first principles study until recently. One reason for the situation is the entanglement problem[28]. The relevant bands may get crossed with the other bands, and it is not easy to separate them. By selecting sets of variable numbers of Bloch functions at every k-point, the entanglement problem can be solved.

One common way to construct Wannier functions[28] is as follows. First, the Bloch wave functions are obtained from the DFT calculation. One then can introduce a trial basis for the Wannier functions.

$$|\phi_{n\mathbf{k}} = \sum_{m=1}^{J} |\psi_{m\mathbf{k}}\rangle\langle\psi_{m\mathbf{k}}|g_n\rangle, \tag{1.13}$$

here $g_n(\mathbf{r})$ are those trial functions.

The overlap is then calculated.

$$(S_{\mathbf{k}})_{mn} = \langle\phi_{m\mathbf{k}}|\phi_{n\mathbf{k}}\rangle = (A_{\mathbf{k}}^{\dagger}A_{\mathbf{k}})_{mn}, \tag{1.14}$$

where $(A_{\mathbf{k}})_{mn} = \langle\psi_{m\mathbf{k}}|g_n\rangle$.

One can then construct the Löwdin-orthonormalized Bloch-like states

$$|\tilde{\psi}_{n\mathbf{k}}\rangle = \sum_{m=1}^{J} |\phi_{m\mathbf{k}}\rangle(S_{\mathbf{k}}^{-1/2})_{mn}. \tag{1.15}$$

After a Fourier transformation (See Eqn.(1.11), one can obtain the Wannier functions. We will use this method later.

1.3 The organization of this thesis

The thesis is organized as follows. To give the readers some flavor of the QSHE and QAHE, we will introduce some models on the ruby lattice, which can host the topological insulating and Chern insulating phases in Chap. two. From Chap. three on, we gradually connect these states to real materials. The third chapter is about a semi-empirical model of thin films of pyrochlore

iridates. From Hartree-Fock studies of these systems, we find topological insulating and Chern insulating phases. In the fourth chapter, starting from a DFT study and Wannier functions, we construct realistic models of those thin films, and further confirm the topological phases. The effectiveness of our approach is discussed. We believe these methods are powerful and our results could bring useful insights for experimentalists.

Chapter 2

Topological phases in the ruby lattice

2.1 Introduction

For a long time, the fractional quantum Hall effect (FQHE) could only be realized in two dimensional electron gas under very low temperature and a strong external magnetic field.[1] However, recently the study of nearly flat bands with non-trivial topology has attracted a lot of attention[29–33]. In those systems, due to the very tiny bandwidth comparing to the gap, weak interactions can drive the system into a strongly correlated regime. If the band is topologically nontrivial and partially filled, the FQHE can occur without an external magnetic field or Landau levels.

In those systems, the topologically nontrivial band must be very flat. The example of those systems includes kagome, checkerboard and so on[29–33]. Most of those systems require models including up to the third neighbor hopping. In those systems, it is hard to obtain a gap to bandwith ratio as large as 50.

---

[1]This chapter is based on the published paper: Xiang Hu, Mehdi Kargarian, Gregory A. Fiete, "Topological insulators and fractional quantum Hall effect on the ruby lattice", Phys. Rev. B **84**, 155116 (2011). Greg Fiete conceived of the project. Mehdi Kargarian performed some calculations. Xiang Hu did most of the calculations. Xiang Hu and Greg Fiete wrote the paper.

However, in this chapter, we will introduce the ruby lattice. The gap to bandwidth ratio in this model can easily reach around 70, even only considering the second neighbor hopping. After fine tuning the parameters, the maximal gap to bandwidth ratio in this model can overceed 100. Among all the models reported up to now, it is the highest. Therefore, the ruby lattice provides an excellent platform for the study of the FQHE. In addition, if the topologically nontrivial flat band is fully occupied, we can obtain the QAHE.

In addition to the nearly flat band, the system also reveals some other salient features, such as a topological insulating phase, if we consider nearest neighbor hopping and second-neighbor spin-orbit coupling.

In this chapter, we first reveal the flat band feature of ruby lattice, with an emphasize on the large gap to bandwith ratio. We then discuss the topological insulating phase by displaying band structures and phase diagrams for different cases.

2.2   Structure

The structure of the ruby lattice is more complicated than the honeycomb or kagome lattice. Basically, the two-dimensional Bravais lattice belongs to triangular type. In other words, the unit cell basis vectors are given by

$$\mathbf{a}_1 = a\hat{x}$$
$$\mathbf{a}_2 = \frac{a}{2}\hat{x} + \frac{\sqrt{3}a}{2}\hat{y}, \tag{2.1}$$
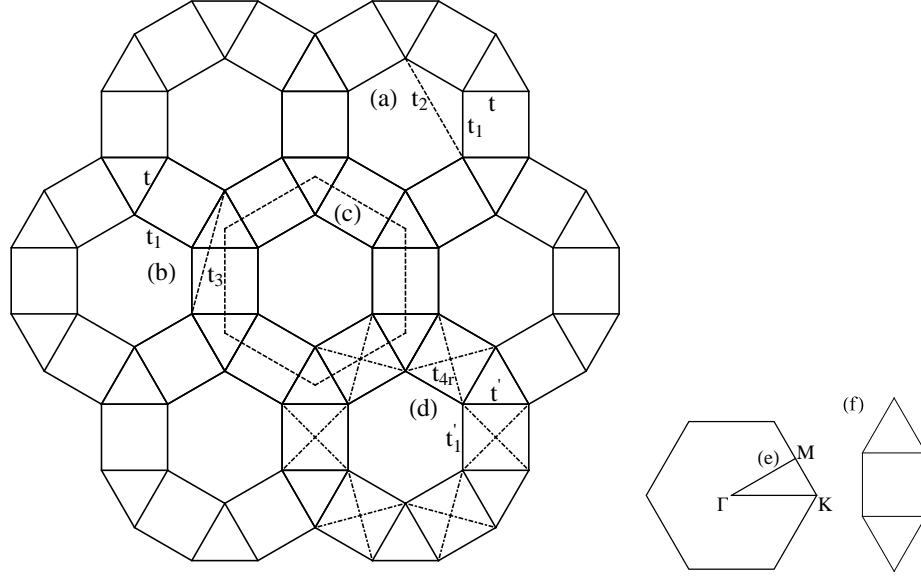
Figure 2.1: The structure of the ruby lattice, and the terms to be used in our models. Here t, t_1 (real) and t', t_1' (complex) are nearest neighbor hopping parameters. The "second-neighbor" SOC strength are indicated as t_2, t_3. t_{4r} is the second neighbor hopping. All those terms are subjected to the lattice symmetry. (a) The spin-orbit coupling within a hexagon whose strength is t_2. (b) The spin-orbit coupling within a pentagon composed of one triangle and one square, whose strength is t_3. (c) The hexagonal unit cell of the ruby lattice. (d) The hopping parameters used to obtain a non-trivial flat band. (e) The 1st Brillouin zone of the ruby lattice. The high symmetric paths are also marked. (f) The unit cell as a "ruby".

here a is the lattice constant, and the reciprocal lattice basis vectors are defined as

$$
\begin{aligned}
\mathbf{b}_1 &= \frac{2\pi}{a}\hat{x} - \frac{2\pi}{\sqrt{3}a}\hat{y}, \\
\mathbf{b}_2 &= \frac{4\pi}{\sqrt{3}a}\hat{y}.
\end{aligned}
\tag{2.2}
$$

In each unit cell, there are six sites, with different ways to select those

12

sites. Of course we can take the Wigner-Seitz unitcell. In this way, the six sites form a hexagon, which preserves the six-fold rotational symmetry of the lattice, as shown in Fig.2.1(c). Comparing to the honeycomb lattice, we can see the major difference is that every vertex in the honeycomb lattice has been extended to a triangle, either pointing upward or downward.

Another way to select the unit cell is to keep one upper triangle and one adjacent lower triangule in one unit cell, as shown in Fig.2.1(f). In this way, the unit cell looks like a ruby. This is the reason why the lattice is called the ruby lattice.

2.3   Hamiltonian and band structure

To study the nearly flat band in the ruby lattice, we start with the spin-polarized case. In this case, the time-reversal symmetry is broken, which is similar to the case of quantum Hall effect.

We then introduce a non-interacting model with complex hopping parameters on the ruby lattice

$$H_0 = -t' \sum_{i,j \in \triangle, \sigma} c_{i\sigma}^\dagger c_{j\sigma} - t'_1 \sum_{\triangle \to \triangle, \sigma} c_{i\sigma}^\dagger c_{j\sigma}, \tag{2.3}$$

with

$$t' = t + \mathrm{i}\sigma_z t_i,$$
$$t'_1 = t_{1r} + \mathrm{i}\sigma_z t_{1i}. \tag{2.4}$$

. In this model, $c_i^\dagger / c_j$ represents the creation/annihilation operator on the

13

site i and j respectively. t' refers to the hopping between the vertices of the hexagons, and t'_1 refers to the hopping between the vertices of the triangles. t_r, t_i, t_{1r}, t_{1i} are some real parameters. The complex hopping can be introducted as the spin-orbit coupling terms, in some strongly correlated systems [34–36]. Another way to realize the complex hopping is through Raman field induced in optical lattices [37–39].

Then the Hamiltonian is diagonalied using standard LAPACK codes. The diagonalization process is equivalent to a transformation of the Hamiltonian in k-space, as

$$H = \sum_{\mathbf{k}} \Psi_{\mathbf{k}}^{\dagger} \tilde{H}_{\mathbf{k}} \Psi_{\mathbf{k}}, \tag{2.5}$$

where $\Psi_{\mathbf{k}}^{\dagger} = (c_{1\mathbf{k}}^{\dagger}, c_{2\mathbf{k}}^{\dagger}, c_{3\mathbf{k}}^{\dagger}, c_{4\mathbf{k}}^{\dagger}, c_{5\mathbf{k}}^{\dagger}, c_{6\mathbf{k}}^{\dagger})$ are defined in the six sites.

After obtaining the band structure, we then can calculate the Chern number of the ground state, which is defined as[32]

$$c_n = \frac{1}{2\pi} \int_{BZ} d^2k F_{12}(k), \tag{2.6}$$

where $F_{12}(k)$ is Berry culvature defined as

$$F_{12}(k) = \frac{\partial}{\partial k_1} A_2(k) - \frac{\partial}{\partial k_2} A_1(k), \tag{2.7}$$

and $A_\mu(k) = -i\langle u_{n\mathbf{k}}|\frac{\partial}{\partial k_\mu}|u_{n\mathbf{k}}\rangle$ is the Berry connection. Here $|u_{n\mathbf{k}}\rangle$ are the Bloch wavefunctions of the nth band. For the study of the ground state only, $n = 1$.

In a real calculation, the above formula is fairly hard to implement. Even if we can mesh the brillouin zone to very fine sizes, it is still very hard

to ensure the numerical integration returns an integer. Therefore, we use the methods introduced in Ref.[40]. The algorithm converts the intergration into a summation in k-space by introducing some $U(1)$ gauge transformation link varibles.

With that method, we search through the parameter space, focusing on those ground states with non-trivial topology. The maximal gap to bandwidth ratio we can obtain with nearest neighbor hopping only is around 13. This value does not satisify the very flat criterion, which usually requires a gap to bandwidth ratio E_g/W around 50.

In order to obtain more flat band, we have to include more hopping terms in the model. For this purpose, we add on the next nearest neighbor hopping in the square next to the hexagons on the ruby lattice, as shown in Fig.2.1(d). With additional term, we find there exist nearly flat band with nontrivial topology. For example, the case when $t_i = 1.2t, t_{1r} = -1.2t, t_{1i} = 2.6t, t_{4r} = -1.2t$. The Chern number is -1 and the gap $= 2.398t$ with band width $= 0.037t$. The corepsonding gap to bandwidth ratio is $E_g/W \approx 64$, which is already a very high number compared to other models. The corresponding band structure is shown in Fig. 2.2.

2.4 The exploration of maximum gap to bandwidth ratio

In this section, we explore the maximum gap to bandwidth ratio our model in the previous section can reach. We begin the exploration by searching
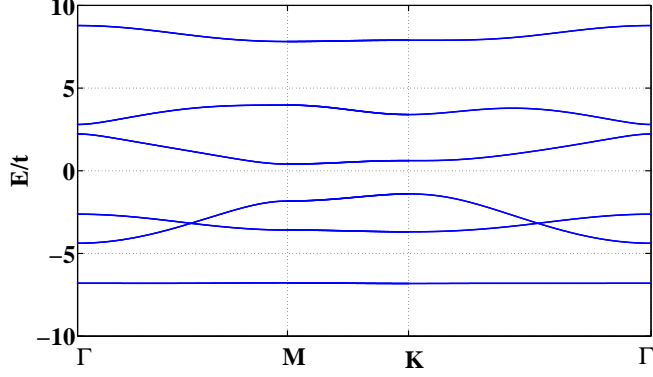
Figure 2.2: The electric structure with $t_i = 1.2t, t_{1r} = -1.2t, t_{1i} = 2.6t, t_{4r} = -1.2t$. We can see the ground state has a very flat band.

through a large scope of parameter space. Using t as the unit for any energy related parameters, we look at the region with $t_i, t_{1r}, t_{1i}, t_{4r}$ between $-4t$ and $4t$, and the step length is $0.1t$. In table 2.1, we list the top 10 largest gap to bandwidth ratios we find in the ruby lattice for the topological nontrivial cases.

Number	t_i/t	t_{1r}/t	t_{1i}/t	t_{4r}/t	G/W
1	3.8	0.5	-1.2	1.3	167.29
2	1.5	2.5	0.7	-1.6	116.44
3	2.9	0.6	-3.9	2.9	114.59
4	2.2	0.6	-3.2	2.2	113.86
5	3	-0.6	4	-3	112.56
6	2.9	-0.3	3.7	-2.9	111.11
7	1.8	0.6	-2.8	1.8	110.63
8	2.6	0.3	-3.4	2.6	110.61
9	1.5	2.3	0.8	-1.6	108.83
10	1.7	0.6	-2.7	1.7	107.29

Table 2.1: The top ten gap to bandwidth ratios.

2.5 The topological insulating phase in the ruby lattice

From this section on, we focus on another topic of our study, that is, the topological insulating phase on the ruby lattice.

The starting point of our study is the Hamiltonian

$$H = H_0 + H_{\text{SO}}, \tag{2.8}$$

where

$$H_0 = -t \sum_{i,j \in \triangle, \sigma} c_{i\sigma}^\dagger c_{j\sigma} - t_1 \sum_{\triangle \to \triangle, \sigma} c_{i\sigma}^\dagger c_{j\sigma}, \tag{2.9}$$

and

$$H_{\text{SO}} = it_2 \sum_{\ll ij \gg, \alpha\beta} \nu_{ij} s_{\alpha\beta}^z c_{i\alpha}^\dagger c_{j\beta} + it_3 \sum_{\ll ij \gg, \alpha\beta} \nu_{ij} s_{\alpha\beta}^z c_{i\alpha}^\dagger c_{j\beta} \tag{2.10}$$

In these equations $c_{i\sigma}^\dagger/c_{i\sigma}$ represents the creation/annihilation operator of an electron on site i with spin σ. t and t_1 are nearest neighbor hopping parameters, and t_2, t_3 are second-neighbor hoppings. All the hopping parameters are real numbers. The quantity ν_{ij} depends on the direction the electron makes a turn at the lattice links of the second-neighbor hopping. When the electron makes a left turn, it is equal to 1, otherwise it is equal to -1.

Because this model preserves the time reversal symmetry and inversion symmetry, all the bands are spin up and down degenerate. We only include the s orbital on each site, so there are six double degenerated bands in the final electronic structure.

We then calculate the bulk band structure without and with SOC, as shown in Fig.2.3. Similar to the honeycomb lattice, when there is no spin-

17
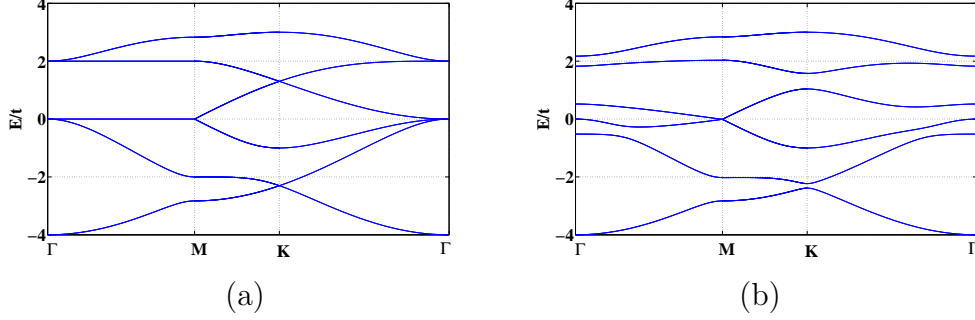
Figure 2.3: The energy bands without and with SOC, given by Eq.(2.8). (a) Bulk energy bands without SOC. We can see Dirac points at K for 1/6 and 2/3 filling. We can also see the quadratic band touching points at Γ for 1/2 and 5/6 filling. (b) The energy bands with SOC turned on, where $t_2 = t_3 = 0.1t$. The Dirac points at the K points and quadratic band touching points at the Γ point are now gapped out.

orbit coupling, in other words, $t_1 = t$, $t_2 = t_3 = 0$, at the Γ point and half filling and 5/6, the systems reveals quadratic touching Dirac points, which are unstable under perturbations. On the other hand, at the K and K' points, Dirac points also occur at $\frac{1}{6}$ filling and $\frac{2}{3}$. We can infer that once spin-orbit coupling is taken into account, it creates gaps at those points. The spin-orbit coupling can also drive band inversion, which will result in some topological phases, and thus non-trivial edge modes.

A stripe geometry calculation verifies these results, as shown in Fig.2.4. We can see non-trivial edge states emerge at $\frac{1}{6}$ and $\frac{2}{3}$ filling, at time reversal invariant points where $k_x = 0$ or $k_x = \pi/a$. Because the Fermi surface crosses the edge states an odd number of times we can look just at one spin component to see if the insulating phase is in fact topological[7, 8].

That is just a special case. To understand this model more thoroughly
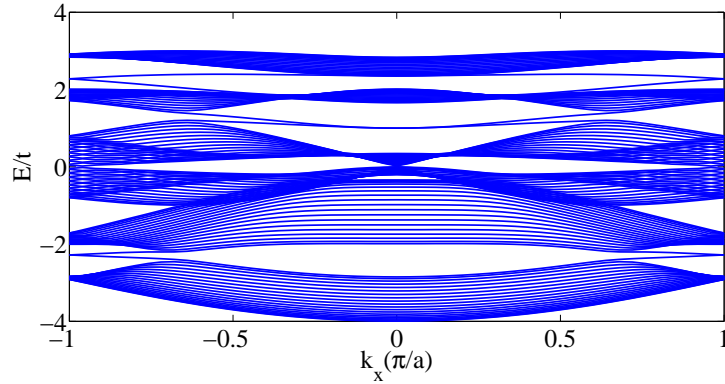
Figure 2.4: The energy bands on a strip geometry with $t_1 = t$, $t_2 = t_3 = 0.1t$. We can see that at the filling fractions 1/6 and 2/3 odd numbers of Dirac cones for each spin component emerge on the edge.

we explore the phase space of a large scope of parameters. First, we will discuss how to determine the phases in a reliable and systematic way.

2.6   Phase diagrams of the model

The determination of the phase with given parameters is based on the following: First, by checking the band structure, one can determine whether the system is insulating or conducting. If the system is insulating, the Z_2 topological number is calculated to determine whether it is topologically non-trivial.

For a given filling fraction, whether it is conducting depends on whether the conduction and valence bands are crossing. In other words, we check whether the top of the valence band is as high as the bottom of the conduction band. The search for the maximum or minimum of a given band is not that

easy, due to the complex band structure of this model. For that purpose, we use an optimization algorithm called the differential evolution method[41]. It is often effective, but has some deficiencies. To double check the results, the software Mathematica is very helpful in determining the extreme values.

The Z_2 invariant is calculated using the Fu-Kane formula[42], due to the inversion symmetry of our model. The eigenvalues of the parity operator at the four time reversal invariant points in the k-space is defined at,

$$\mathbf{b} = \frac{n_1}{2}\mathbf{b}_1 + \frac{n_2}{2}\mathbf{b}_2, \tag{2.11}$$

where

$$n_1, n_2 = 0, 1. \tag{2.12}$$

And the Z_2 topological class can be calculated as[42]

$$(-1)^\nu = \prod_{a=1}^{4} \delta_a, \tag{2.13}$$

where

$$\delta_a = \prod_{m=1}^{N} \xi_{2m}(\Gamma_a). \tag{2.14}$$

Here Γ_a is a time reversal invariant point, and $\xi_{2m}(\Gamma_a)$ is the eigenvalue of the parity operator of the $2m$-th occupied state at the time reversal invariant point Γ_a.

Since the hopping parameters t, t_1, t_2, and t_3 can all be tuned, a large parameter space exists. To understand the effect of each parameter more clearly, it is beneficial to cut through the three-dimensional parameter space to explore the phase diagrams. In the following, we discuss different ways of slicing.

2.6.1 Phase diagrams for $t_2 = t_3$

In this section, we fix the second neighbor hopping values $t_2 = t_3 = \lambda_{\mathrm{SO}}$ in (2.10). The spin orbit coupling λ_{SO} is the same all over the lattice. On the other hand, the inter-triangle hopping t_1 is tuned.

The different phases are represented by the different colors:

Black=Conductor, Grey=Insulator, White=Topological Insulator.
As Fig. 2.5 shown, for filling fractions 1/6, 1/3, 1/2, 2/3, and 5/6, the rich physics is shown in those diagrams.
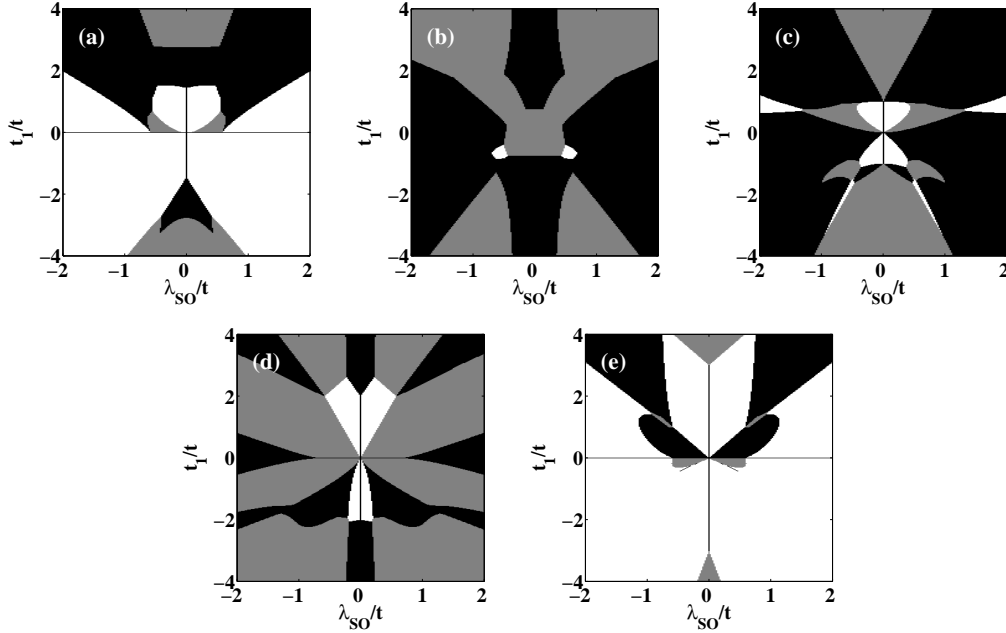
Figure 2.5: Phase diagrams for different fractions from 1/6 to 5/6. In figures (a)-(e), the filling fraction are increased by 1/6 each time. The black color represents conductors, and grey is for trivial insulators, while white is for topological insulators. In those figures, $t_2 = t_3 = \lambda_{\mathrm{SO}}$ and t_1 are shown respectively in the horizontal and vertical axes, in units of t.

21

We can see some overall trends on those phase diagrams. First, all the above phase diagrams has the symmetry about $\lambda = 0$. This is easy to understand, because if we reverse the sign of λ_{SO}, the phase does not change. Because the system has inversion and time reversal symmetries, the above transformation is equivalent to spin flip, which does not change the dispersion relation, so the phase remains the same.

Second, for $\frac{1}{6}$ and $\frac{5}{6}$ fillings, the topological insulating phases occupy the widest areas on the phase digram. That is not surprising, since the quadratic or linearly touching Dirac points has been found for those filling fraction in the bulk energy bands with $t_2 = t_3 = 0$. For the other filling fractions, the topological insulating phases are mostly separated stripes. Due to the lack of Dirac cones in the bulk structure, this is expected.

Also on figure (a), (b), (c), (d), the middle and the vertical axes remain gray or black. With $\lambda_{\text{SO}} = 0$, the middle vertical axes in these phase diagrams are impossible to be topological insulating. This is because in our model, only the SOC can drive band inversion and then cause the topologically non-trivial phase. The horizontal straight line on the phase diagram represents the conducting phase.

For $\frac{1}{2}$ filling the phase diagram appears rather complex. Narrow regions around $\lambda_{\text{SO}} = \pm 0.7t$ and $t_1 = -2.0t$ are still topological insulating.

2.6.2 Phase diagrams for fixed t_1

The previous section shows the effect of spin-orbit coupling in the formation of topological insulating phase. We then focus on the effects of those two types of spin-orbit couplings, t_2, t_3. The hopping between triangles t_1 is fixed. We study the competetion and cooperation between the two types of spin-orbit coupling t_2 and t_3.

The phase diagrams for $t_1 = 0$ and $t_1 = t$ are shown in Figs. 2.6-2.7.

The phase diagrams illustrated in Fig. 2.6 in which $t_1 = 0$ are a special case. For any filling fraction with $t_1 = 0$, the origin is a trivial insulator. That is easy to understand since no hopping occurs in this model, which is similar to the case of a lot of isolated atoms. For 1/6, 1/2 and 5/6 fillings, most areas are metallic. While for 1/3 and 2/3 fillings, the metallic and insulating phases both occupy around one half of the total region.

The phase diagrams for $t_1 = t$ reveals some salient features. The large spread of topolgical insulating phase with filling fraction 1/6 and 5/6 is in a contrast with the absence of a topological insulating phase with filling fractions 1/3 and 2/3. We emphasize the 2/3 filling case. Although in Fig. 2.3(a), the bands at filling fraction 2/3 both has a Dirac cone at the K-point, the phase diagram does not show abundant region of topological insulator. Therefore, the existence of Dirac cone without SOC is not a gurantee for topologial insulator when SOC is turned on. The relationship between them should be more complicated. Similar cases are found when spin-orbit coupling emerges
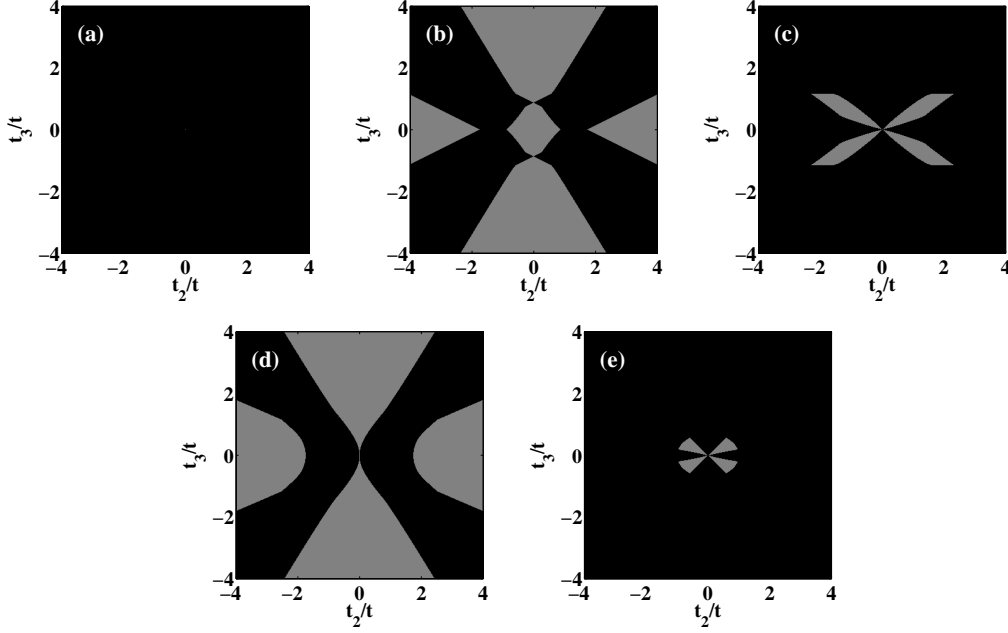
Figure 2.6: Phase diagrams for $t_1 = 0$. In figures (a)-(e), the filling fraction are increased by $1/6$ each time. The black color represents conductor, and grey is for trivial insulator, while white is for opological Insulator. In those figures, t_2 and t_3 are shown respectively in the horizontal and vertical axes, in units of t. The origin $t_2 = t_3 = 0$ is always a trivial insulator.

from interactions.[43–47]

Another feature is the symmetry of the phase diagrams. If the signs of any two among t_1, t_2, and t_3 are reversed, the phase of the system remains the same. The flip of the signs of t_1 and t_3 can be absorbed via a simple gauge transformation of electron operators defined as $c^\dagger(c) \to -c^\dagger(-c)$ for up triangles and $c^\dagger(c) \to c^\dagger(c)$ for down triangles. Flipping the signs of t_2 and t_3 can also be absorbed into the magnetic fields for different spin species, i.e. $\nu_{ij} \to -\nu_{ij}$, which does not change the dispersion relation and the phase.

24
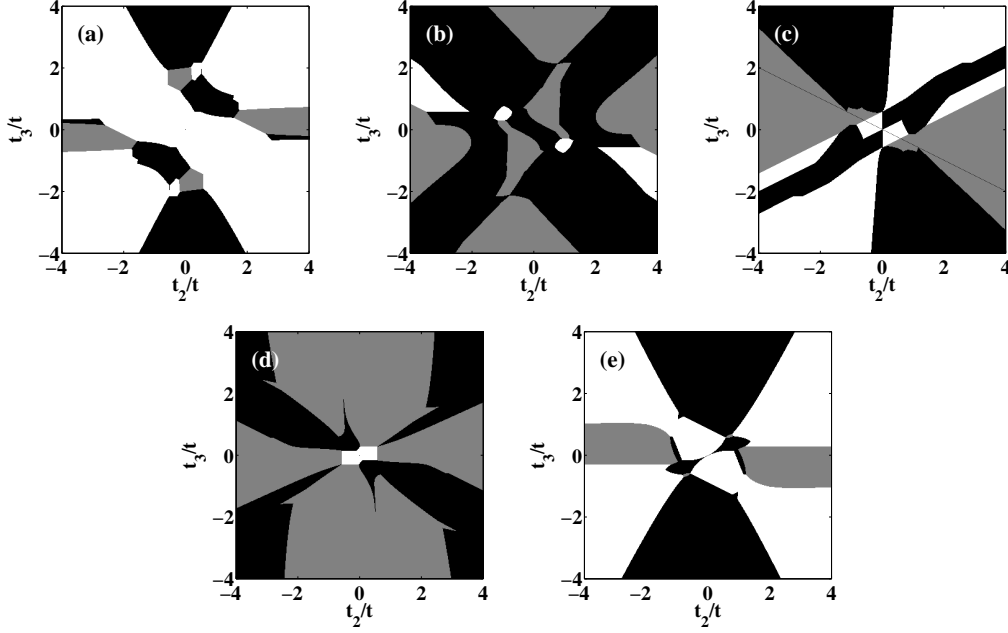
Figure 2.7: Phase diagrams for $t_1 = t$. In figures (a)-(e), the filling fraction are increased by $1/6$ each time. The black color represents conductor, and grey is for trivial insulator, while white is for topological Insulator. In those figures, t_2 and t_3 are shown respectively in the horizontal and vertical axes, in units of t.

We can also have a look at $t_1 = 2t$ case. When the filling fraction is $\frac{5}{6}$, if $t_2 = t$ and $t_3 = 0$, or $t_2 = 0$ and $t_3 = 0.4t$, the system is topological. If we increase t_2 to t, and keep $t_3 = 0.4t$, the system is a metal. In this case, the two types of spin-orbit coupling are competing against each other in driving the topological insulating phase. However, they can support each other in some other cases. The competetion and supporting can be explained by the fact that the inner effective magnetic field created by those two types of spin-orbit coupling can compete against or support each other.
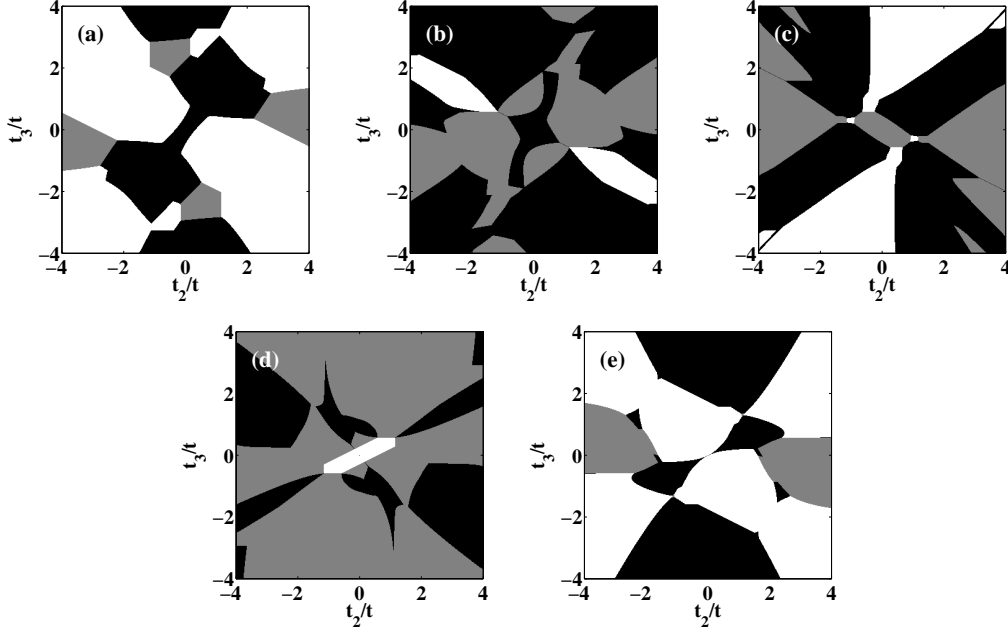
Figure 2.8: Phase diagrams for $t_1 = 2t$. In figures (a)-(e), the filling fraction are increased by 1/6 each time. The black color represents conductor, and grey is for trivial insulator, while white is for topological Insulator. In those figures, t_2 and t_3 are shown respectively in the horizontal and vertical axes, in units of t.

2.7   Conclusion and discussion

In this charpter, we introduced the ruby lattice which can host topologically non-trivial nearly flat bands and the topological insulating states. The large gap to bandwidth ratio indicates it is a very good model to study FQHE. The numerical verification of the FQHE phase has been carried out by some other groups.

The disadvantage of this model is that it lacks connection to real materials, although it is possible to realize in optical lattices [48–54]. Searching

for the real material to realize the ruby lattice, or even its deformed version is still an open question.

Chapter 3

Thin films of pyrochlore iridates: a semi-empirical model

3.1 Introduction

In the previous chapter, we discussed a tight-binding model on the ruby lattice[55]. That is just one example of a topological phases in theoretical models. Our goal is to find those states in real materials.[1] Up to now, a bunch of topological materials have been discovered[9–23]. However, most of those materials suffer from large bulk conductivity and the Fermi surface shifting over time[56]. Strictly speaking, those materials are still not really topological "insulating". The obvious bulk conductivity brings a lot of inconvenience both to laboratory study and industrial application. For example, in transport experiments, it is not very easy to differentiate the bulk contribution apart from the contribution of surface states[57].

Therefore, the study of topological phases in oxides begin to attract more and more attention[58–64]. The large bulk resistivity in a lot of oxides

---

[1]Chapter three is based on the published paper: Xiang Hu, Andreas Rüegg, Gregory A. Fiete, "Topological phases in layered pyrochlore oxide thin films along the [111] direction", Phys. Rev. B **86**, 235141 (2012), Editor's suggestion. Greg Fiete conceived of the project. Andreas Rüegg performed some calculations. Xiang Hu did most of the calculations. The three authors wrote the paper.

provides a possiblity to realize topological "insulating" phases. Most efforts focus on transition metal oxides with perovskite or pyrochlore structure.

Band inversion caused by intrinsic or effective SOC is usually important for the formation of topological states. In transition metal oxides with $3d$ valenace electrons, the intrinsic SOC of those transition metal ions, although small, can be magnified by strong localization effect[58, 65]. On the other hand, effective SOC[35, 36] also emerges from interactions, as is easy to see from a simple mean field treatment. While in transition metal oxides with $5d$ valence electrons, like iridates, the intrinsic SOC is comparable with correlation strength. The interplay of SOC and correlation give rise to very rich physics. Up to now, a lot of novel states such as topological insulators, Chern insulators, Weyl semi-metals have been predicted in the iridates[59, 64, 66]. However, despite numerious experimental studies, these predictions have not been proved by any experiment in bulk iridates[58].

The study of graphene can illuminate us a lot. After defoliating from the bulk structure (graphites), the two dimensional stucture reavels the potential to many different topological phases[7]. If we can defoliate the transition metal oxides into many layers, we can also possibly create some new topological materials[35, 36, 65, 67–75].

However, in those transition metal oxides, due to the transition metal ions residing in the center of some cages of oxygen ions, the thin film of those materials must be sandwiched in some substrates and capping layers to create stable heterostructures[35, 36, 67, 68, 76].

Although the [001] direction is a natural cleavage direction of perovskites, it is not the most favorable direction for the emergence of topological states[77–85]. In thin films of perovskites grown along the [111] direction[35, 36, 67, 68, 76], band structure calculation reveals quadratic band touching at the Γ point, which is unstable under perturbations. On the other hand, they may host nearly flat bands, whose large density of states may also drive unstability. In both case, band inversion can be induced, and topological phases may emerge. In spite of these salient features, the experimental growth of perovskites along the [111] direction is still so tricky that only a few experimental results are known[86–88].

In this chapter, we will study thin films of pyrochlore iridates. The formula of bulk pyrochlore iridates is $A_2Ir_2O_7$[59, 60, 64, 66]. Here A is some kind of rare earth element such as Y, La, and Ce. Usually, the A ion has little effect on the electric structure close to Fermi surface, although its size affects the lattice parameter. The Bravais lattice of pyrochlore belongs to face-centered cubic. In each unit cell, there are 22 ions, including four A ions, four iridium ions, and 14 oxygen ions, with those iridium ions form a tetrahedron. The bulk pyrchlore structure is inversion symmetric. In addition, the [111] direction is a natural cleavage direction, which may bring convenience to the preparation of thin films along that direction. In the following, we will introduce the thin film structures along the [111] direction, and determine their phases in the non-interacting and interacting cases.

3.2 Structure of the thin films along [111] direction

As Fig.3.1, shown, along the [111] direction, the pyrochlore thin films of iridates forms alternating layers of kagome and triangular lattices. By changing the thickness of the thin film, we can obtain different structures. Here we focus on four different types of thin films: (i) a single kagome layer, (ii) a triangular-kagome bilayer, (iii) a triangular-kagome-triangular trilayer (TKT), and (iv) a kagome-triangular-kagome trilayer (KTK), as are shown in Fig. 3.2.
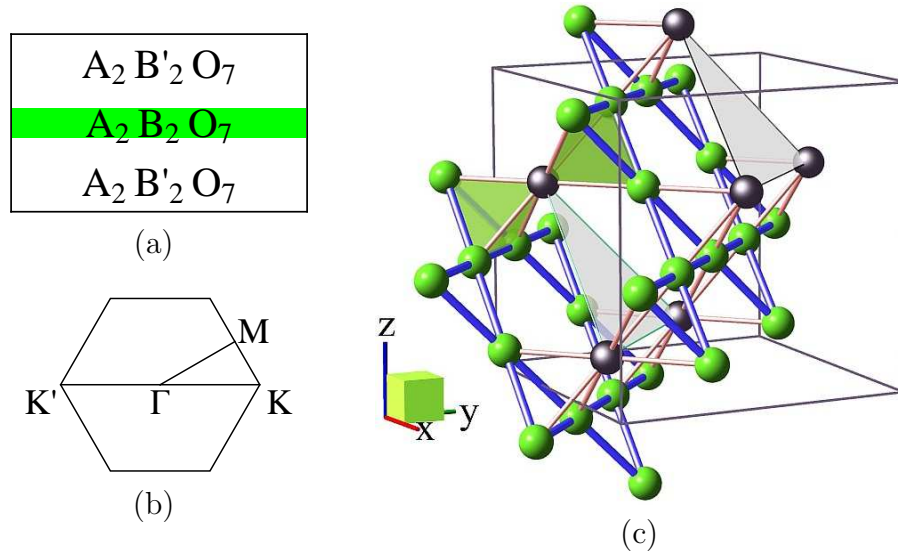
Figure 3.1: (color online) (a)The $A_2B'_2O_7/A_2B_2O_7/A_2B'_2O_7$ sandwich structure. (b) The first Brillouin zone of the thin films. (c) Pyrochlore lattice structure. Alternating kagome and triangular lattice planes stack along the [111] direction. The green atoms locate in the kagome planes and grey atoms sit in the triangular planes.

As we point out previously, to stablize their structure, the thin films have to be sandwiched in some substrate and capping layers, which are chosen as $A_2B'_2O_7$, as shown in Fig.3.1(a). Those capping layers are some trivial band

insulators with large gaps. They created an environment similar to vaccum. However, by changing the composition of the capping layer we can also apply different strain on the thin films, and potentially create new phases.

In the pyrochlore lattice, each B ion inhabit in an octaheral cage of oxygen ions. Therefore, it is under a cubic crystal field which split the $5d$ orbitals into t_{2g} and e_g manifolds[89]. The $t_{2g} - e_g$ splitting can be up to 2-3eV in the iridates. Due to the large energy difference, we can focus on the t_{2g} manifolds if we consider filling number less or equal to 6 for each iridium ion.
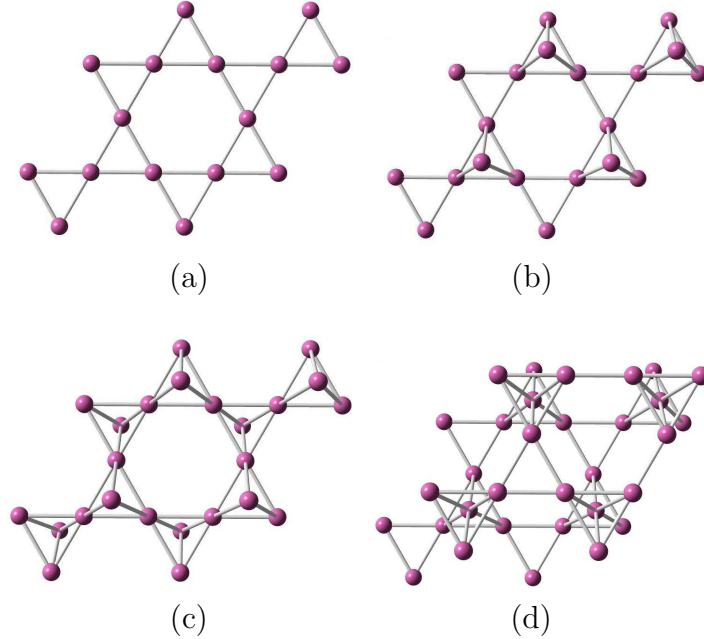
Figure 3.2: Single, double, and triple layer thin films along [111] directions. (a) Single kagome layer. (b) Bilayer. (c) Triangular-kagome-triangular (TKT) trilayer. (d) Kagome-triangular-kagome (KTK) trilayer.

In the t_{2g} manifold, the effective orbital angular meomentum is defined as $P_{t_{2g}} \mathbf{L} P_{t_{2g}} = -\mathbf{l}_{l=1}$. Here $P_{t_{2g}}$ is the projection operation into the t_{2g} sub-

space. Due to the existence of the minus sign in the effective orbital angular momentum, the onsite SOC for t_{2g} manifold is $\sim \lambda(-\mathbf{l}) \cdot \mathbf{s}$. From that we can see that the $j = 1/2$ manifold lies above the $j = 3/2$ manifold. The splitting depends on the value of λ.

3.3 The non-interacting model

We start with a tight-binding model defined in the t_{2g} manifold.

$$H_0 = \sum_{\langle i,j \rangle, \alpha, \beta} t_{i\alpha, j\beta} c_{i\alpha}^{\dagger} c_{j\beta} - \lambda \sum_i \mathbf{l}_i \cdot \mathbf{s}_i, \tag{3.1}$$

where the $5d$-orbital hopping is [63, 66]

$$t_{i\alpha, j\beta} = t_{i\alpha, j\beta}^{in} + t_{i\alpha, j\beta}^{dir}. \tag{3.2}$$

Here $c_{i\alpha}^{\dagger}$ and $c_{i\beta}$ are respectively the electron creation and annilation operators on site i. α and β are state indexes which include both spin and orbital information. t represents the hopping strength. Comparing to $3d$ orbitals, the $4d$ and $5d$ orbitals are already rather extended. There are two possible ways for the electron to jump from one site to the other. One basic way is by hopping through the intermediate oxygen ions, which is indirect hopping[59, 60, 90]. The other way is for the electron wave function to overlap directly, resulting in the direct hopping terms [63, 66].

The construction of the hopping term can be established in the standard Slater-Koster(SK)[91] way. However, as the local t_{2g} orbits can be decomposited into the linear combination of all the $5d$ orbitals, the SK matrix elements

33

have to be constructed in the general coordinates, and then rotated to the local coordinates.

The rotational matrices M_i are 5×3 matrices given by

$$
M_1 = \begin{pmatrix} -2/9 & -5/9 & 2/9 \\ -5/9 & -2/9 & 2/9 \\ -2/9 & -2/9 & 5/9 \\ 2/(3\sqrt{3}) & 2/(3\sqrt{3}) & 4/(3\sqrt{3}) \\ 2/3 & -2/3 & 0 \end{pmatrix} ,
\tag{3.3}
$$

$$
M_2 = \begin{pmatrix} -2/9 & -2/9 & 5/9 \\ 2/9 & 5/9 & -2/9 \\ 5/9 & 2/9 & -2/9 \\ -4/(3\sqrt{3}) & 2/(3\sqrt{3}) & -2/(3\sqrt{3}) \\ 0 & 2/3 & 2/3 \end{pmatrix} ,
\tag{3.4}
$$

$$
M_3 = \begin{pmatrix} 5/9 & 2/9 & -2/9 \\ -2/9 & -2/9 & 5/9 \\ 2/9 & 5/9 & -2/9 \\ 2/(3\sqrt{3}) & -4/(3\sqrt{3}) & -2/(3\sqrt{3}) \\ -2/3 & 0 & -2/3 \end{pmatrix} ,
\tag{3.5}
$$

$$
M_4 = \begin{pmatrix} 5/9 & 2/9 & -2/9 \\ 2/9 & 2/9 & -5/9 \\ -2/9 & -5/9 & 2/9 \\ 2/(3\sqrt{3}) & -4/(3\sqrt{3}) & -2/(3\sqrt{3}) \\ -2/3 & 0 & -2/3 \end{pmatrix} .
\tag{3.6}
$$

The corresponding basis is the local yz, xz, xy orbitals and $yz, xz, xy, 3z^2 - r^2, x^2 - y^2$ orbitals in general coordinates.

The direct hopping between local t_{2g} orbitals from site j to site i is defined as

$$
t_{i\alpha,j\beta}^{dir} = M_i^T S_{dd}(\hat{e}_{ij}) M_j \otimes \left(D_i^\dagger D_j \right)_{\alpha\beta} ,
\tag{3.7}
$$

where D_i is the SU(2) rotational spin matrix[59, 60, 90].

The indirect hopping terms can be obtained in a similar way. But one has to remember it is a second order process which occurs between the $5d$ orbitals of iridium ions and the $2p$ orbitals of oxygen ions.

We consider only the σ and π bond for the direct hopping. The corresponding hopping strengths are represented by t_s and t_p, respectively. In all our studies, we follow the convention[63, 66] that the $t_p = -2/3 * t_s$, and the indirect hopping strength t is set as the basic unit of energy in this charpter.

In the local t_{2g} basis with spin $(yz \uparrow, yz \downarrow, xz \uparrow, xz \downarrow, xy \uparrow, xy \downarrow)$, the SOC term $-\lambda \mathbf{l}_i \cdot \mathbf{s}_i$ has the format

$$
\lambda \begin{pmatrix}
0 & 0 & 0.5i & 0 & 0 & -0.5 \\
0 & 0 & 0 & -0.5i & 0.5 & 0 \\
-0.5i & 0 & 0 & 0 & 0 & 0.5i \\
0 & 0.5i & 0 & 0 & 0.5i & 0 \\
0 & 0.5 & 0 & -0.5i & 0 & 0 \\
-0.5 & 0 & -0.5i & 0 & 0 & 0
\end{pmatrix}
$$

Using results that we obtained in chapter 4, we can estimate the indirect hopping strength to be 0.2-0.4 eV, while the SOC strength is 0.4-0.5eV. In our study, we study two cases with $\lambda/t = 2, 4$.

3.4   Non-interacting solutions

Next, we calculate the energy bands for different thin films. We determine the phase of the thin films in the following way. First, we study whether the system is conducting or insulating. This can be determined by observing if the bottom of the conduction band is as low as the top of the valence band. Following this, the Z_2 topological number is calculated.
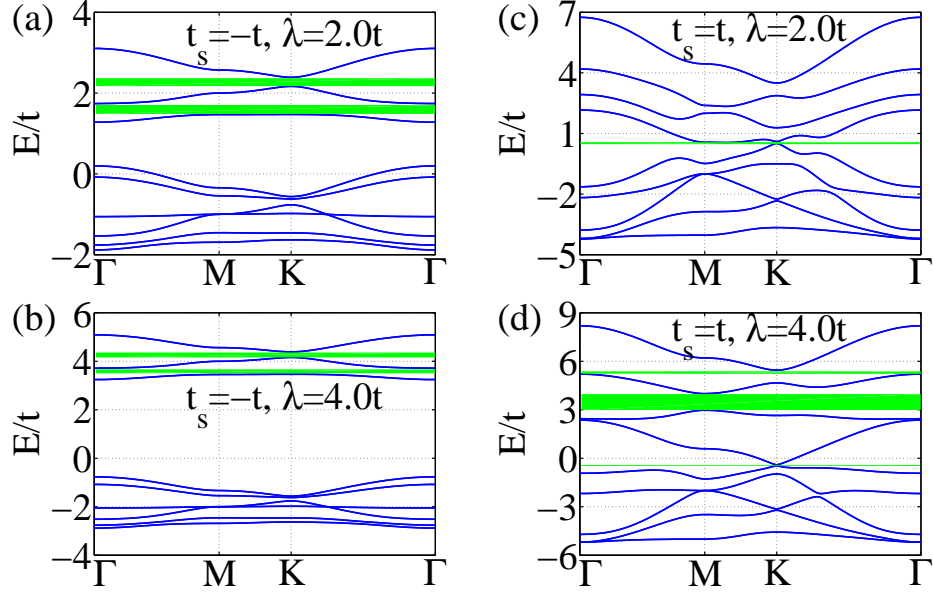
Figure 3.3: The band structure of Eq. (3.1) of a single kagome layer. The tuning parameters are shown on the figures. Green (light grey) lines whose widths are equal to the corresponding indirect gaps indicate filling fractions of t_{2g} manifold to realize the Z_2 topological insualting phase: (a) $\frac{7}{9}$, $\frac{8}{9}$; (b) $\frac{7}{9}$, $\frac{8}{9}$; (c) $\frac{5}{9}$; (d) $\frac{5}{9}$, $\frac{7}{9}$, $\frac{8}{9}$.

In the single layer, TKT or KTK cases, the systems withhold inversion symmetry. The Z_2 topological number can be calculated with the Fu-Kane formula[42]. In the bilayer case, due to the breaking of inversion symmetry, we have to use a different algorithm based on the Fukui formula[92]. In this formula, the wave functions in the meshed Broullion zone must abide by time reversal symmetry. We then convert the integration to summation in the formula.

Our main results for the band structure are shown in Figs. 3.3-3.6. In the single layer case, the results are similar to the kagome lattice. Due to dif-
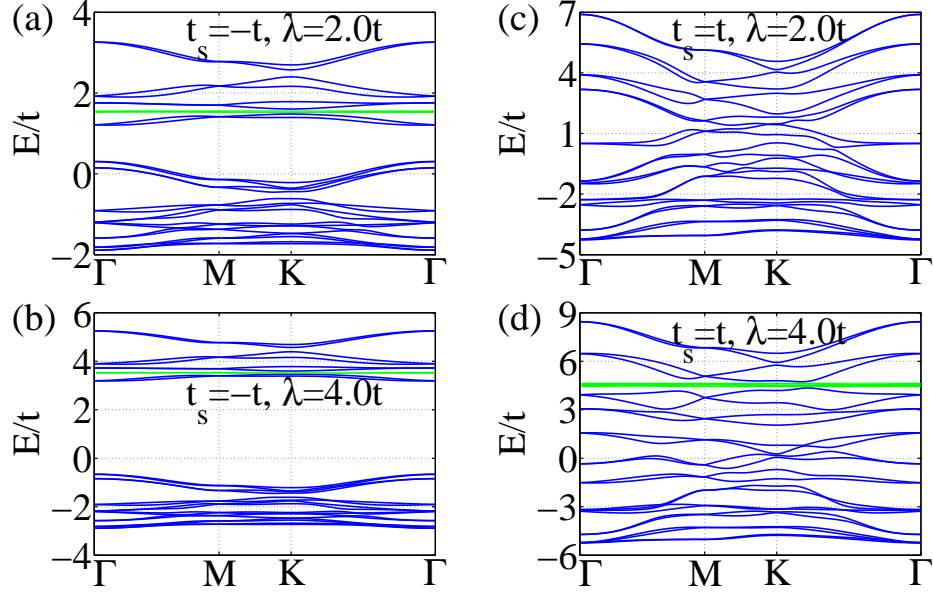
Figure 3.4: The band structure of Eq. (3.1) of bilayer. The tuning parameters are shown on the figures. Green (light grey) lines whose widths are equal to the corresponding indirect gaps indicate filling fractions of t_{2g} manifold to realize the Z_2 topological insualting phase: (a) $\frac{3}{4}$; (b) $\frac{3}{4}$; (d) $\frac{5}{6}$.

ferent format of hopping, the nearly flat band in the s orbital model on kagome lattice is no longer seen. In the bilayer case, the system no longer reveals inversion symmetry, so the energy bands are no longer spin degenerated. In the TKT and KTK case, the bands are more complicated. In addition, we can see that a large λ does not necessary result in the well separation between j=1/2 and j=3/2 manifold. With $t_s = t$, they are not separated even for $\lambda = 4t$.

The filling fractions (in t_{2g} orbitals) favorable for topological insulating phases are shown by the green color bar in each band figure. We can see that the only filling fraction that can be naturally realized without doping the film
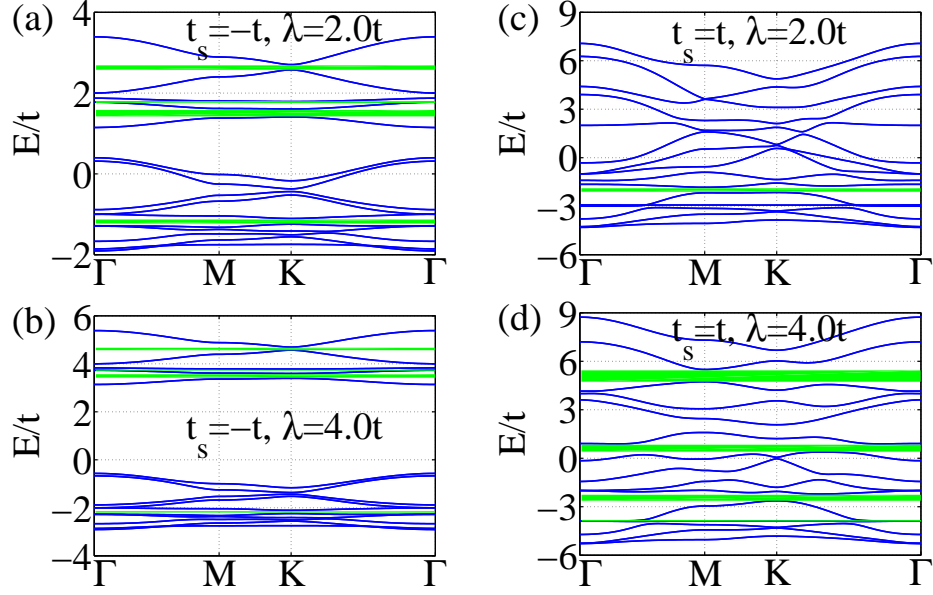
Figure 3.5: The band structure of Eq. (3.1) of a TKT trilayer. The tuning parameters are shown on the figures. Green (light grey) lines whose widths are equal to the corresponding indirect gaps indicate filling fractions of t_{2g} manifold to realize the Z_2 topological insualting phase: (a) $\frac{1}{3}$, $\frac{11}{15}$, $\frac{4}{5}$, $\frac{14}{15}$; (b) $\frac{1}{3}$, $\frac{11}{15}$, $\frac{4}{5}$, $\frac{14}{15}$; (c) $\frac{1}{3}$; (d) $\frac{4}{15}$, $\frac{1}{3}$, $\frac{3}{5}$, $\frac{13}{15}$.

is the bilayer case with $t_s = t$. To further study it, we search through all the possible combinations of t_s and t_p and draw the phase diagrams.

3.5 Non-interacting phase diagrams

Previously, we followed the convention of previous studies and assumed $t_p = -2/3 * t_s$. In real materials, whether this assumption is correct is still an open question, so it is necessary to study other cases. Here we show the $t_s - t_p$ phase diagrams. We can see the value of λ/t does matter. When λ/t is equal to 4, the region of topological insulators is much larger than when it

38
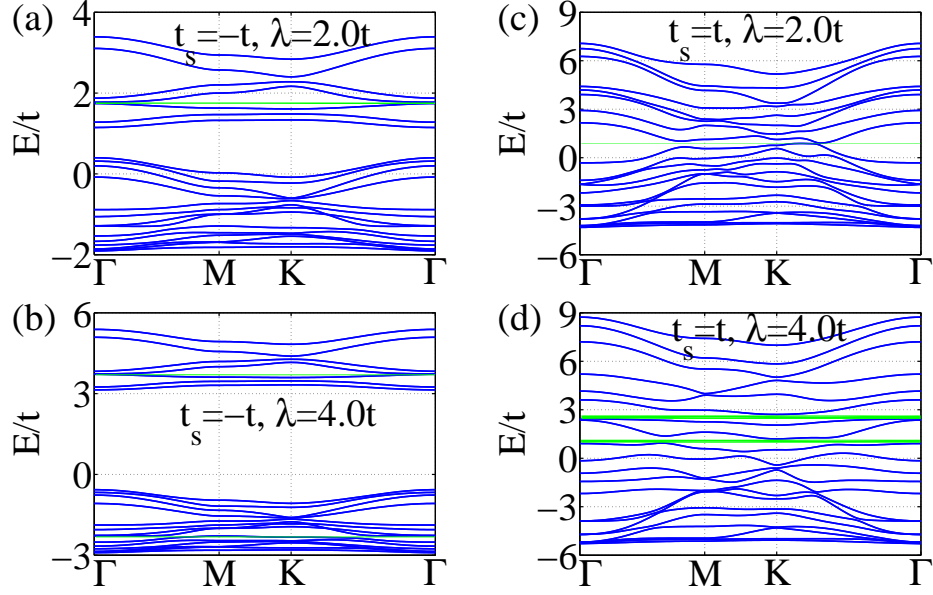
Figure 3.6: The band structure of Eq. (3.1) of a KTK trilayer. The tuning parameters are shown on the figures. Green (light grey) lines whose widths are equal to the corresponding indirect gaps indicate filling fractions of t_{2g} manifold to realize the Z_2 topological insualting phase: (a) $\frac{17}{21}$; (b) $\frac{2}{7}$, $\frac{17}{21}$; (c) $\frac{13}{21}$; (d) $\frac{13}{21}$, $\frac{15}{21}$.

is 2. This can be expected since the SOC plays an important role driving the system into topological insulating.

3.6 The interacting case

Previously, we studied the non-interacting case. In this section, we will turn to the interacting case.

For the convenience of our study, we use the strong SOC approximation, and our model is defined in the $j = 1/2$ manifold by a direct projection into the subspace. The effectiveness of this picture has to be justfied. In the next
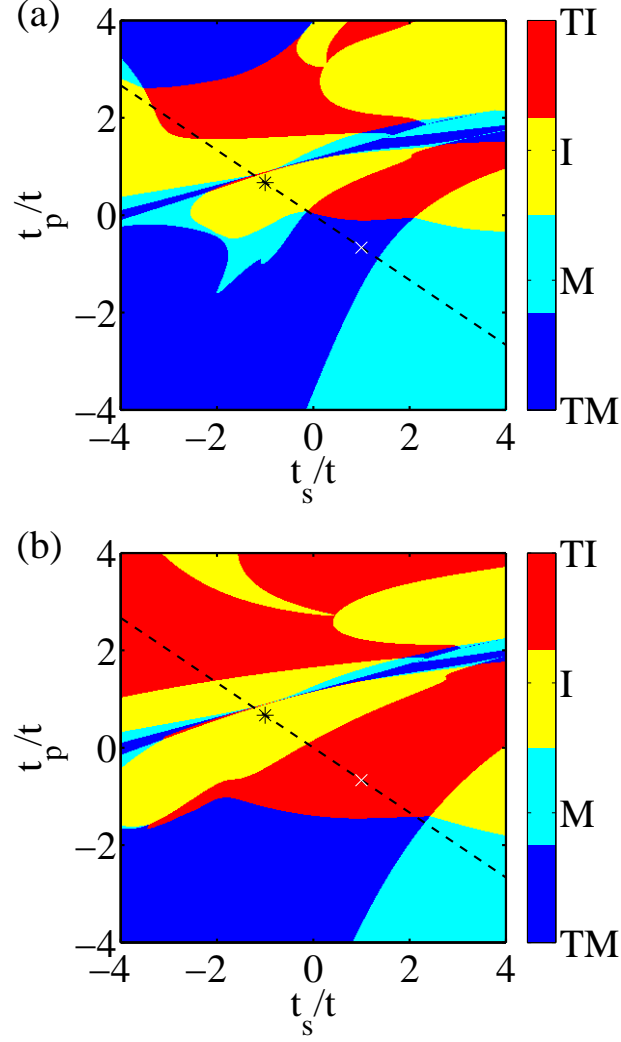
Figure 3.7: Phase diagrams for the bilayer thin film at $5/6$ filling in the t_{2g} manifold. (a) $\lambda = 2t$ and (b) $\lambda = 4t$. TM represents a Z_2 topological metal (non-trivial Z_2 index for bands under the direct gap), M is a metal. I represents a trivial insulator, and TI is a topological insulator. On the black line with $t_p = -2t_s/3$, the $*$ is (-1, 2/3) and the $\times$ is (1, -2/3), which correspond to the two values of $t_s = \pm 1$ shown in Figs. 3.3- 3.6.

40

chapter we will see, even for a realistic SOC strength, the $j = 1/2$ and $3/2$ bands do not cross directly, so the mixing between them is not significant. For that reason, we can still use the $j = 1/2$ picture.

The model is established by adding a Hubbard U term to Eq. (3.1) in the pseudospin basis of $j = 1/2$. As the zero-th order approximation, the tight-binding part is obtained by projecting all the hopping terms directly into the $j = 1/2$ subspace. That treatment is eqivalent to setting λ to be infinite. The interacting term in the model is the following:

$$H_U = U \sum n_{i\uparrow} n_{i\downarrow}, \tag{3.8}$$

where $\uparrow, \downarrow$ refer to the doublet in the $j = 1/2$ manifold. Because the filling fraction of Ir^{4+} in the t_{2g} manifold is $5/6$, we consider the half-filling interacting case.

3.7   The derivation of Hartree-Fock approximation

The multi-band Hubbard model is difficult to solve. Therefore, we turn to an approximational method. The Hartree-Fock(HF) approximation is one of the easiest ways to decouple the interaction term. The Hartree-Fock approximation is derived in the following way.

For each site, the interacting part is

$$H_U^i = U n_{i\uparrow} n_{i\downarrow}, \tag{3.9}$$

and in the particle number basis, it is

$$H_U^i = U d_\uparrow^\dagger d_\uparrow d_\downarrow^\dagger d_\downarrow, \tag{3.10}$$

where $d^\dagger$ and d represent the pseudospin creation and annihilation operators on the i-th site.

The Hartree part is

$$H_U^{i;h} = U \langle d_\uparrow^\dagger d_\uparrow \rangle d_\downarrow^\dagger d_\downarrow + U d_\uparrow^\dagger d_\uparrow \langle d_\downarrow^\dagger d_\downarrow \rangle - U \langle d_\uparrow^\dagger d_\uparrow \rangle \langle d_\downarrow^\dagger d_\downarrow \rangle, \tag{3.11}$$

and the Fock part is

$$H_U^{i,f} = -U \langle d_\downarrow^\dagger d_\uparrow \rangle d_\uparrow^\dagger d_\downarrow - U d_\downarrow^\dagger d_\uparrow \langle d_\uparrow^\dagger d_\downarrow \rangle + U \langle d_\downarrow^\dagger d_\uparrow \rangle \langle d_\uparrow^\dagger d_\downarrow \rangle. \tag{3.12}$$

Defining

$$\mathbf{j}_i = \frac{1}{2} \sum_{\alpha\beta=\uparrow,\downarrow} d_{i\alpha}^\dagger \sigma_{\alpha\beta} d_{i\beta}, \tag{3.13}$$

we can then substitute

$$
\begin{aligned}
\langle d_\uparrow^\dagger d_\uparrow \rangle &= \frac{n}{2} + j_z, \\
\langle d_\downarrow^\dagger d_\downarrow \rangle &= \frac{n}{2} - j_z, \\
\langle d_\uparrow^\dagger d_\downarrow \rangle &= j_x + i j_y, \\
\langle d_\downarrow^\dagger d_\uparrow \rangle &= j_x - i j_y,
\end{aligned}
\tag{3.14}
$$

into the approximation, and obtain

$$H_U^i = U \langle \mathbf{j} \rangle^2 - \frac{1}{4} U n^2 + U (d_\uparrow^\dagger d_\downarrow^\dagger) \begin{pmatrix} \frac{n}{2} - j_z & -j_x + i j_y \\ -j_x - i j_y & \frac{n}{2} + j_z \end{pmatrix} \begin{pmatrix} d_\uparrow \\ d_\downarrow \end{pmatrix}. \tag{3.15}$$

42

One of the major differences between the above formula and Ref.[66] is that in their study, they neglected the difference of electron occupation number on each site. This is reasonable in the bulk case, due to the tetragonal symmetry of the unitcell. However, in the thin film case, that symmetry no longer exists. For the sites in the kagome plane and the one(s) in the triangular plane, their occupation numbers must be different, due to the stronger repulsion of electrons inside the kagome plane. On the other hand, if the density difference is too large, it will cause the second term in Eqn. 3.15 to raise. Therefore, the increase of the occupation difference results in energy rising.

In the real calculation of thin films, for simplification, we also neglect the difference of occupation number on each site. This approximation shifts the phase boundaries but does not remove the topological phases.

3.8   The self-consistent calculation

The HF calculation is carried out in an unrestricted self-consistent way. The self-consistent calculation starts from twenty sets of randomly generated initial magnetic configurations $\langle \mathbf{j} \rangle^{in}$. The Brillouin zone is meshed to 150 by 150. The Fermi energy is calculated to make sure the model is half-filled, then the new local magnetic moments $\langle \mathbf{j} \rangle^{out}$ are evaluated on each site. We regard the following criterion

$$|\langle \mathbf{j} \rangle_{i,n}^{in} - \langle \mathbf{j} \rangle_{i,n}^{out}| < 10^{-8}, \tag{3.16}$$

where $n = x, y, z$, as the criterion for the iteraction to converge.

The final converged configuration with the minimum total energy is regarded as the ground state. For $|\langle \mathbf{j} \rangle| < 0.01$, we treat the phase as non-magnetic and reset the magnetic moments to zero.

3.9   The phase diagrams

We determine the phase of the interacting case in a similar way as the non-interacting case. However, for the magnetic insulators, the Chern number is calculated using Fukui's algorithm[40].

All the phase diagrams are shown in Fig.3.8.

There are a few key points in these figure to be emphasized. First we can see the critical value of U in each structure of film agrees with the approximated bandwidth of the $j = 1/2$ manifold. That is not hard to understand since the Stoner's criterion can be applied.

In the single, TKT and KTK cases, the weakly interacting case proves to be metallic. As U increases, the systems first become pseudospin non-degenerated. In that case, the film is still conducting as long as the two spin components are not well-separated. Finally, if U is large enough, the system becomes magnetic insulating.

In the bilayer case, the filling fraction makes it insulating for the small U. In addition, after calculating the Z_2 topological number, we can verify it is topological insulating, which is consistent with the non-interacting case.

In all those cases, if $U > 3t$, the film appears magnetic insulating.

44
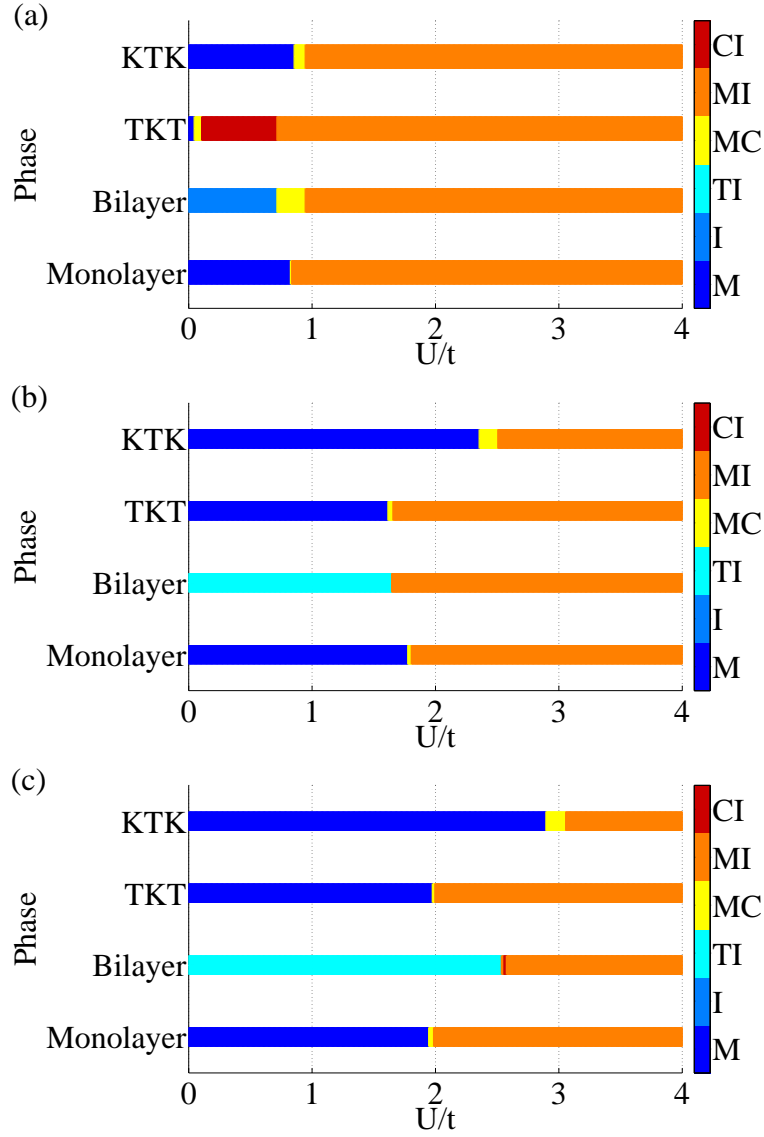
Figure 3.8: The phases of the interacting model with(3.8). (a) $t_s = -t$, (b) $t_s = 0.25t$, and (c) $t_s = t$ for 1/2 filling. On the figures, M is a metal, I represents a trivial insulator. TI is a topological insulator. MC is a magnetic conductor, and MI is a trivial magnetic insulator, and CI is a Chern insulator (QAHE state).

In the bilayer case, the case $t_s = t$ is special. For small U, it appears as a topological insulator. While for a large enough interaction strength, the system first becomes magnetic insulating. As U increases, two tendencies compete with each other. On the one hand, the splitting between the upper and lower Hubbard bands causes the gap to increase. On the other hand, the magnetic moments created by interaction act like an onsite Zeeman field, which results in different energy shifting for different pseudospin components. At first, the magnetic moments increases fast as U increases, so the gap between the valence and conduction band shrinks, cause the gap to close at around $U/t = 2.5$. Once the gap reopens, due to a small perturbation of changing parameter, the system is Chern insulating since the Chern number of the valence and conduction bands have exchanged with each other. But the Chern insulator does not cover a wide region. As U increases further, the valence and conduction bands touch and separate again, turning the system into trivial magnetic insulating. From the second time the gap closes and reopens onward, the gap always increases because the splitting Hubband bands now plays the main role.

Although the bilayer thin film is able to host both topological insulating and Chern insulating phases for different U values, the TKT trilayer thin film is also attractive, since for $U < t$ region there is a wide area of Chern insulators. This is closely connected to the emergence of the nearly flat band for $t_s = -t$ case.

3.10 Magnetic configurations

It is interesting to look at the magnetic configures for different cases. As we expected, the sign of t_s has an important impact on the magnetic order, similar to the three-dimensional studies.[66] While all the magnetic moments are non-coplanar, and the net magentic moments in one unitcell is nonzero, the configuration can be divided into two kinds: one reveals the C_3 rotational symmetry and the other not, as shown in Figs.3.9-3.10.
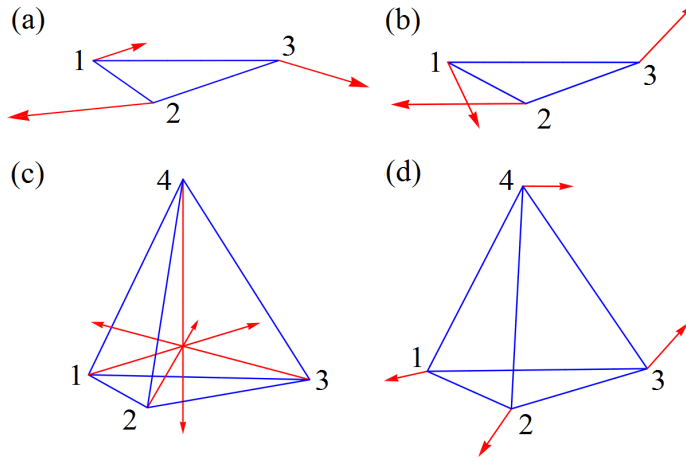
Figure 3.9: Magnetic configurations obtained within the Hartree-Fock approximation for a single kagome layer with (a) $t_s = -t, U = 2.5t$, (b) $t_s = t, U = 3.0t$ and a bilayer with (c) $t_s = -t, U = 3.0t$, (d) $t_s = t, U = 3.0t$.

3.11 Discussion and conclusions

Based on a multi-band Hubbard model, we study the different types of thin films of pyrochlore iridates, and find that the bilayer and TKT trilayer thin films can possibly host topological insulating or Chern insulating phases.

47
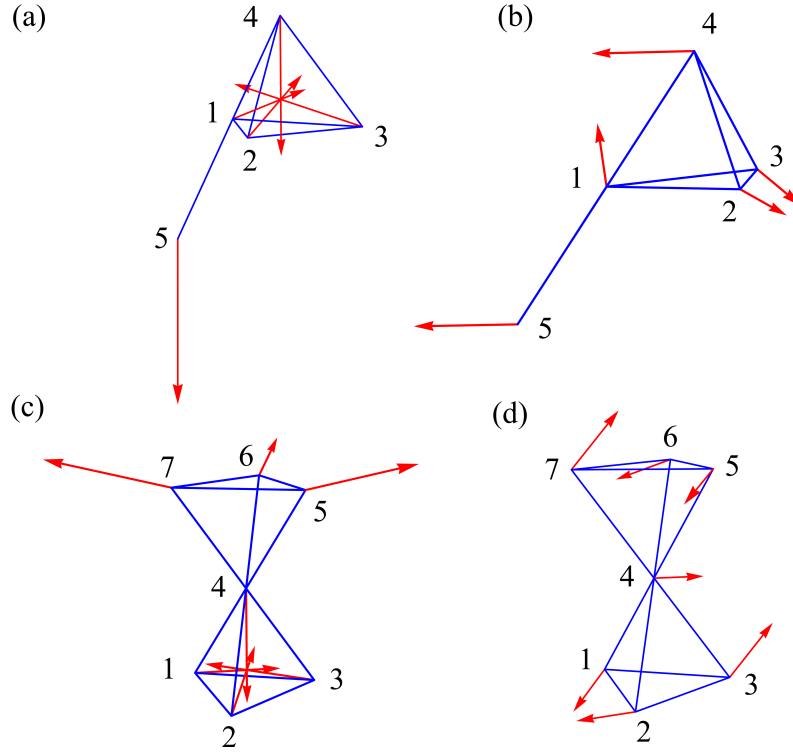
Figure 3.10: Magnetic configurations for a TKT layer: (a) $t_s = -t, U = 3.0t$, (b) $t_s = t, U = 3.0t$ and for a KTK layer: (c) $t_s = -t, U = 2.5t$, (d) $t_s = t, U = 3.0t$.

These predictions will help experimentalists search for new topological materials, including quantum anomalous Hall insulators.

Our predictions rely on the effectiveness of $j = 1/2$ picture in pyrochlore iridates, and we make some assumptions about the hopping parameters. To obtain a realistic model for the real material, and to determine the scope of topological phases more accurately, one needs to use the first principles calculation to determine more realistic energy bands. This is accomplished in the next chapter.

Since the Hartree-Fock approximation only considers the static correlaton effects, the effect of quantum fluctuation also needs to be addressed further. In a recent paper [93], the authors investigate the fluctuation effect with dynamic mean field theory. Their results verify the existence of these topological phases in our study, and in addition, the fluctuation enhances the topological phases instead of destroying them.

Chapter 4

Thin films of pyrochlore iridates: first principles study

4.1 Introduction

Previously, we studied thin films of pyrochlore iridates grown along the [111] direction[75]. Our study was based on a semi-empirical tight-binding model. In this chapter[1], we use a first-principles DFT calculation[64] to obtain a realistic tight-binding model, and then carry out a Hartree-Fock calculation based on it[94].

4.2 Bulk density functional theory calculation

Our basic strategy is the following: first we obtain a tight-binding model for the bulk pyrochlore iridates, then we apply the tight-binding model to the thin films by a slab-truncation. This strategy proves to be effective in the study of a bunch of topological insulators, so we believe it also works in the films we study here. For the purpose of further verification, at the later

---

[1]This chapter is based on the published paper: Xiang Hu, Zhicheng Zhong, Gregory A. Fiete, "First Principles Prediction of Topological Phases in Thin Films of Pyrochlore Iridates", Sci. Rep. **5**, 11072 (2015). Greg Fiete and Xiang Hu conceived of the project. Zhicheng Zhong performed some calculations. Xiang Hu did most of the calculations. Greg Fiete and Xiang Hu wrote the paper.

part of this chapter, we also give some results based on a tight-binding model obtained directly from the first-principles calculation of the thin film, and show that approach yields results very similar to the slab-truncation approach.

We obtain the bulk structure of $Y_2Ir_2O_7$ from Ref.[95]. In this structure, each iridium ion is subjected to a cubic crystal field. Two parameters are essential for the determination of the position of all ions in a pyrochlore lattice, that is, the lattice constant a and the position parameter of some oxygen ions x. In an ideal pyrochlore structure, the value of $x = x_c$ should be 5/16. In that case, the B ion is under a perfect cubic crystal field. If $x \neq x_c$, the oxtahedral cage of oxygen ions is compressed or stretched in the *local* [111] direction. That compression causes the t_{2g} manifold to split into a_{1g} and e'_g manifolds. In our case, in the bulk $Y_2Ir_2O_7$ structure, the value $x = 0.3356$ which is greater than x_c, so the oxygen cages are compressed.

Our density functional theory calculations are carried out in the `WIEN2k`[96] package by using the all-electron full-potential augmented plane-wave method, and in the `Quantum Espresso`(QE) [97] package using a norm-conserving pseudopotential. In both packages, generalized gradient approximation (GGA) of exchange-correlation density functional is used, and the SOC of each type of ion is considered in a fully-relativistic scheme. In both band calculations, the self-consistent part is carried out with a $10 \times 10 \times 10$ Monkhost-Pack[98] k-grid. In QE, the pseudopotentials are generated with the intrinsic `ATOMIC` package, and the valence configuration selections are:

Y ($[Kr]4d^1 5s^2$) : $4s, 4p, 4d, 5s, 5p$;

Ir $([Xe]4f^{14}5d^76s^2)$: $5s, 5p, 5d, 6s, 6p$;

O $([He]2s^22p^4)$: $2s, 2p$.

To enhance the transferability of the pseudopotentials, we include the semi-core states, that is, $4s, 4p$ in Y, and $5s, 5p$ in Ir valence configurations. The cutoff energy in QE calculation was selected to be 150 Rydberg (Ry) for plane waves, and 600 Ry for charge densities. In `WIEN2k`, there is no need for pseudopotentials as all orbitals are used in the calculation. The other parameters in `WIEN2k` are just selected as default. Our results show that the band structure obtained from those two different ways are very close to each other.

4.3 The failure of the fitting method

To obtain a realistic tight-binding model, we first write the necessary hopping terms, and then determine the hopping parameters through a fitting to the DFT band structure. A similar strategy has been proved to be successful in the study of $3d$ transition metal compounds[67, 99].

Our tight-binding model includes the direct hopping between nearest neighbors, second neighbors and third neighbors, and indirect hopping between nearest neighbors. All the hopping terms are generated using SK[91] integrals. Although the model includes so many terms, the fitting to DFT results is still poor in quality. The agreement is not too bad for the $j = 1/2$ part, however, the deviation is obvious for the $j = 3/2$ bands.

The failure of the fitting method reminds us that the $5d$ orbitals are much more extended than $3d$ orbitals. To obtain a reasonable tight binding model, one needs to include even more terms, which is not realistic by hand. Therefore, we turn to the systematic method, that is, the Wannier projection.
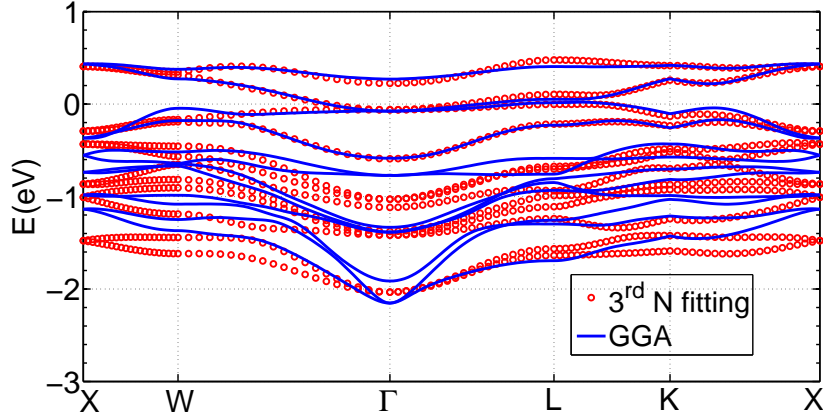
Figure 4.1: The tight-binding fitting to a GGA calculation in `WIEN2k`. The tight-binding model include up to the 3rd neighbor hopping.

4.4   Tight-binding model in the basis of Wannier functions

In this section, we use the method introduced in chapter one to construct a tight-binding model for bulk $Y_2Ir_2O_7$ without interaction. The DFT results are transmitted to `Wannier90`[100] through some message interfaces, then a Hamiltonian is constructed in the basis of Wannier functions.

The large spin-orbit coupling has to be added to our non-interacting model. There are two ways for the inclusion. The first way is to try a DFT

calculation and Wannier fit without spin, and then add the onsite spin-orbit coupling "by hand". The strength of SOC is obtained by fitting the Wannier+SOC(tuning the strength by fitting) bands to GGA+SOC bands[70, 100]. This method gives an acceptable agreement. The second way is to include the spin directly in our Wannier functions[100]. For this purpose, one has to pay attention to the gauge selection of those Wannier functions, and make sure the tight-binding parameters abide by the crystalline symmetry of the pyrochlore lattice.

The spin-dependent Wannier fitting is carried out in package `Wannier90`. On each site, the trial wave functions are selected as the *local* t_{2g} orbitals, and the local coordinates of the initial basis are selected as[100]

$$x_1 = (2/3, -1/3, 2/3),$$
$$z_1 = (-2/3, -2/3, 1/3);$$
$$x_2 = (2/3, -2/3, 1/3),$$
$$z_2 = (1/3, 2/3, 2/3);$$
$$x_3 = (1/3, 2/3, -2/3),$$
$$z_3 = (2/3, 1/3, 2/3);$$
$$x_4 = (1/3, -2/3, 2/3),$$
$$z_4 = (2/3, -1/3, -2/3). \tag{4.1}$$

All the Wannier functions are centered on the iridium ions.

The spin quantization direction is selected as the *default*. In order
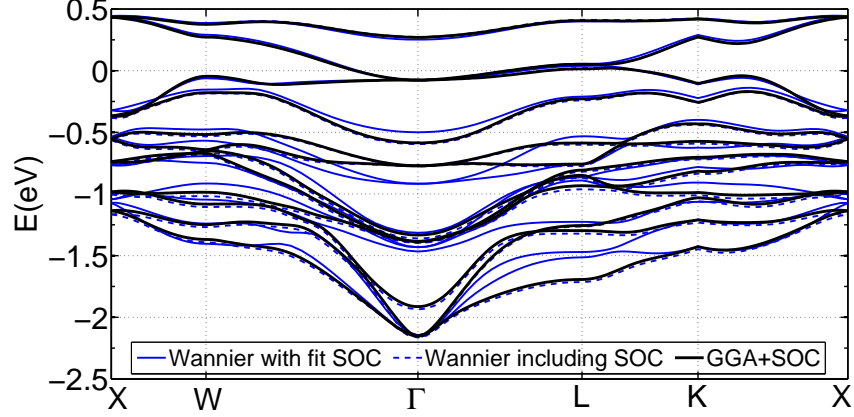
Figure 4.2: The two approaches to incorporate the SOC to the tight-binding Hamiltonian. The dotted blue curves show the band structure from a spin-resolved Wannier projection, while the solid blue curve is obtained by spinless Wannier projection + SOC term whose strength is determined by fitting to the GGA+SOC results (the black curves). The black curves were obtained through `WIEN2k`. All the Wannier projections were done in `QE`+`Wannier90`.

to preserve the lattice symmetry, we do not select the Maximally Localized Wannier Functions, instead, we set NUM_ITER to zero (See appendix).

The results of Wannier fitting is shown in Fig.4.2. The agreement is very well. We notice that if the cut-off magnitude of hopping term is selected as 0.1meV, the hopping between iridium ions almost three times the lattice constant away still needs to be considered. That is an evidence that the $5d$ orbitals are very extended.

4.5   From bulk model to film model

Having established the bulk tight-binding model, we now apply it to thin films by slab-truncation, and then compare it with a direct DFT calculation in the superlattice of sandwich structures shown in Fig.4.3.
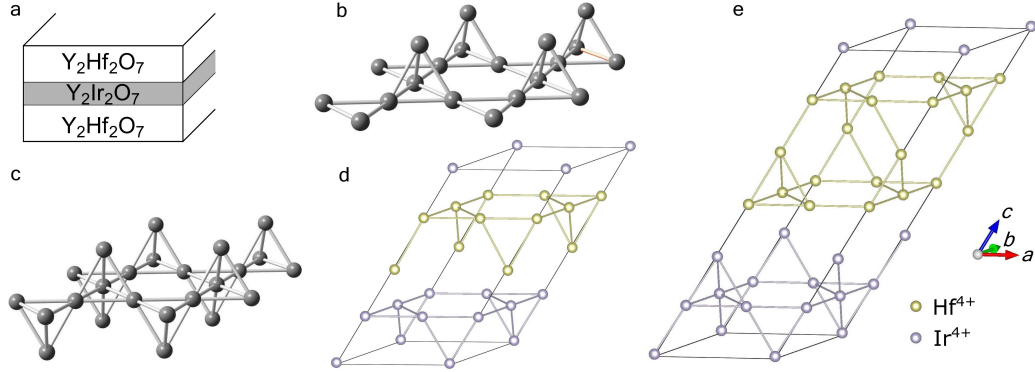
Figure 4.3: The structure of thin films. (a) "Sandwich" structure in real preparations. (b) Bilayer thin film. (c) Triangular-kagome-triangular(TKT) thin film. (d) Relaxed superstructure of bilayer thin film in DFT calculation. (e) Relaxed superstructure of TKT thin film in DFT calculation. Only the Ir^{4+} and Hf^{4+} ions are displayed.

The superlattice $(Y_2Ir_2O_7)_n/(Y_2Hf_2O_7)_m$ includes n Ir^{4+} and m Hf^{4+} layers. For the $n = 2, m = 2$ bilayer thin film, the basis vectors of the superlattice are selected as

$$\mathbf{a} = \mathbf{a}_3 - \mathbf{a}_1,$$

$$\mathbf{b} = \mathbf{a}_2 - \mathbf{a}_1,$$

$$\mathbf{c} = -2 * \mathbf{a}_1,$$

where

$$\mathbf{a}_1 = (0, a/2, a/2),$$

$$\mathbf{a}_2 = (a/2, 0, a/2),$$

$$\mathbf{a}_3 = (a/2, a/2, 0),$$

and a is the lattice constant. The vector $\mathbf{c}$ contains a component out of the (111) plane, while $\mathbf{a}$ and $\mathbf{b}$ reside within the plane. The sandwich structure is obtained by substituting Ir^{4+} ions in two adjacent layers with Hf^{4+} ions (Fig.4.4).

The initial lattice constant a is equal to the average of $Y_2Hf_2O_7$[101] and $Y_2Ir_2O_7$. We construct the unrelaxed trilayer film structure ($n = 3, m = 3$) in a similar way.
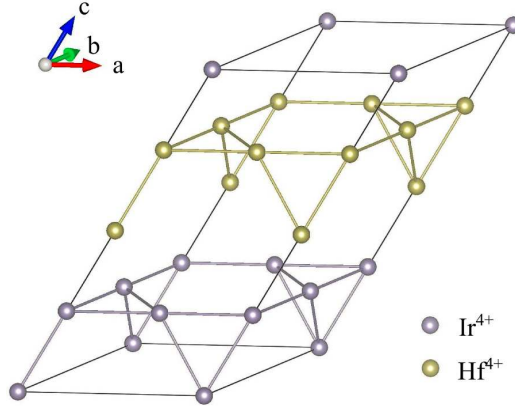
Figure 4.4: The unrelaxed superlattice for bilayer thin film. Note only the Ir^{4+} and Hf^{4+} ions are shown.

The pseudopotential of Hf (with atomic configuration $[Xe]4f^{14}5d^26s^2$) is generated with the valence configuration $5s, 5p, 5d, 6s$, and $6p$. We mesh the

k-space in a 7×7×1 Monkhost-Pack grid[98].

The superlattices are then fully relaxed with scalar-relativistic pseudo-potentials[102]. After the relaxation, their structures are calculated in a fully relativistic basis.

The thin film tight-binding model gives band structures fairly close to the DFT calculation, as shown in Fig.4.5. In the TKT trilayer case, the agreement is very good. In the bilayer case, some deviation occurs. One of the obvious differences is that in the tight-binding model, one can see some band crossings close to the Fermi surface at K points. However, in the DFT results, those crossings are gapped out, but they do not affect the calculation of topological invariants if the direct gap is always open.
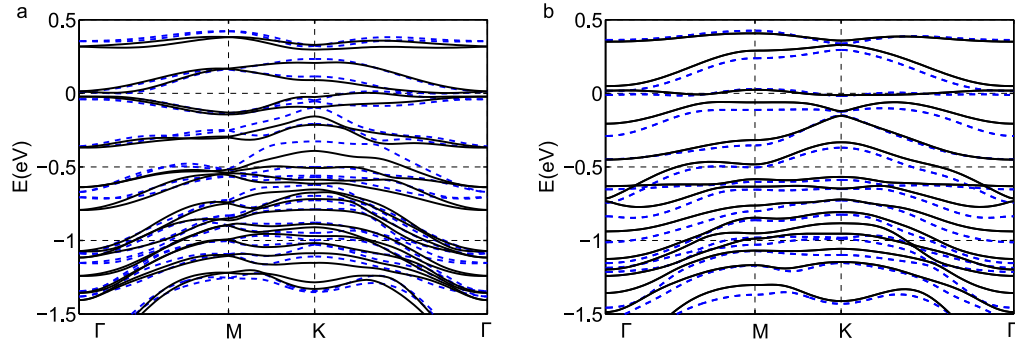
Figure 4.5: Comparison between bands from supercells DFT calculation and a slab-truncation of the bulk model. (a) Bilayer case. (b) TKT trilayer case. The DFT results are obtained from a fully relaxed GGA+SOC calculation (solid black). The slab-truncated model (dashed blue) is the non-interacting part of the Hartree-Fock calculation in thin films.

4.6 Interacting model of thin films and Hartree-Fock approximation

We then add the interaction term to the tight-binding model. The complete expression for our model in the local t_{2g}-like basis is

$$H_0 = \sum_{i,j,\alpha,\beta} \tilde{t}_{i\alpha,j\beta} c_{i\alpha}^\dagger c_{j\beta}, \tag{4.2}$$

$$H_U = \frac{U}{2} \sum_i \left(\sum_\alpha \hat{n}_{i\alpha} - 5 \right)^2, \tag{4.3}$$

where $c_{i\alpha}^\dagger$ $(c_{i\alpha})$ is the creation (annihilation) operator of an electron on site i with orbital α (α, β are orbital indexes including spin indices) in the local t_{2g} manifold. The SOC is included in the complex hopping amplitude $\tilde{t}_{i\alpha,j\beta}$. The interaction part follows the convention of Ref.[60].

The format of the Hubbard term is rotationally invariant (in orbital and spin space), The calculation in the previous chapter relies on the strong SOC approximation, and works only in the $j = 1/2$ subspace. In comparison, our work here is carried out in the whole t_{2g} manifold, which is closer to the realistic case, since the SOC strength is finite (0.4-0.5eV). We neglect the Hund's coupling, because the iridium ions have low-spin configurations[64, 103].

To solve the model, we apply the Hartree-Fock approximation. The

derivation process is as follows:

$$
\begin{aligned}
H_U & = \frac{U}{2} \sum_i \left(\sum_\alpha \hat{n}_{i\alpha} - 5 \right) \left(\sum_\beta \hat{n}_{i\beta} - 5 \right) \\
& = \frac{U}{2} \sum_i \left(\sum_{\alpha\beta} \hat{n}_{i\alpha}\hat{n}_{i\beta} - 10 \sum_\alpha \hat{n}_{i\alpha} + 25 \right).
\end{aligned} \tag{4.4}
$$

Using the condition that the total number of electrons in one unit cell is a constant, or

$$
\sum_{i\alpha} \hat{n}_{i\alpha} = \texttt{constant}, \tag{4.5}
$$

for the ground state, we can throw away the constant part, and obtain

$$
H_U = \frac{U}{2} \sum_i \sum_{\alpha\beta} \hat{n}_{i\alpha}\hat{n}_{i\beta}. \tag{4.6}
$$

Now we divide it into two parts, with $\alpha = \beta$ and $\alpha \neq \beta$.

$$
\frac{H_U}{\frac{U}{2}} = \sum_{i\alpha} \hat{n}_{i\alpha}^2 + \sum_{i\alpha\beta, \alpha\neq\beta} \hat{n}_{i\alpha}\hat{n}_{i\beta}, \tag{4.7}
$$

because $\hat{n}_{i\alpha}^2 = \hat{n}_{i\alpha}$ for the Fermion number operator, we can throw it away, then

$$
\frac{H_U}{\frac{U}{2}} = \sum_{i\alpha\beta, \alpha\neq\beta} \hat{n}_{i\alpha}\hat{n}_{i\beta}. \tag{4.8}
$$

We consider the direct part and the exchange part at mean-field level.

Firstly, the direct part is

$$
\begin{aligned}
\frac{H_U^D}{\frac{U}{2}} & = \sum_{i\alpha\beta, \alpha\neq\beta} \left(n_{i\alpha}\hat{n}_{i\beta} + \hat{n}_{i\alpha}n_{i\beta} - n_{i\alpha}n_{i\beta} \right) \\
& = \sum_{i\alpha\beta, \alpha\neq\beta} \left(2n_{i\alpha}\hat{n}_{i\beta} - n_{i\alpha}n_{i\beta} \right).
\end{aligned} \tag{4.9}
$$

60

Secondly, the exchange part is

$$
\begin{aligned}
\frac{H_U^E}{\frac{U}{2}} &= \sum_{i\alpha\beta,\alpha\neq\beta} \left[\hat{c}_{i\alpha}^\dagger \hat{c}_{i\alpha}(1 - \hat{c}_{i\beta}\hat{c}_{i\beta}^\dagger) \right] \\
&= \sum_{i\alpha\beta,\alpha\neq\beta} \left[\hat{n}_{i\alpha} - \hat{c}_{i\alpha}^\dagger \hat{c}_{i\alpha}\hat{c}_{i\beta}\hat{c}_{i\beta}^\dagger \right].
\end{aligned} \tag{4.10}
$$

Throwing the constant term away, we obtain

$$
\begin{aligned}
\frac{H_U^E}{\frac{U}{2}} &= - \sum_{i\alpha\beta,\alpha\neq\beta} \left[\hat{c}_{i\alpha}^\dagger \hat{c}_{i\alpha}\hat{c}_{i\beta}\hat{c}_{i\beta}^\dagger \right] \\
&= \sum_{i\alpha\beta,\alpha\neq\beta} \left[\hat{c}_{i\alpha}^\dagger \hat{c}_{i\beta}\hat{c}_{i\alpha}\hat{c}_{i\beta}^\dagger \right] \\
&= - \sum_{i\alpha\beta,\alpha\neq\beta} \left[\hat{c}_{i\alpha}^\dagger \hat{c}_{i\beta}\hat{c}_{i\beta}^\dagger \hat{c}_{i\alpha} \right].
\end{aligned} \tag{4.11}
$$

Define $\hat{m}_{\alpha\beta}^i = \hat{c}_{i\alpha}^\dagger \hat{c}_{i\beta}$, then

$$
\begin{aligned}
\frac{H_U^E}{\frac{U}{2}} &= - \sum_{i\alpha\beta} \left(\hat{m}_{\alpha\beta}^i \hat{m}_{\beta\alpha}^i \right) \\
&= - \sum_{i\alpha\beta} (m_{\alpha\beta}^i \hat{m}_{\beta\alpha}^i + \hat{m}_{\alpha\beta}^i m_{\beta\alpha}^i - m_{\alpha\beta}^i m_{\beta\alpha}^i) \\
&= - \sum_{i\alpha\beta} \left(2m_{\alpha\beta}^i \hat{m}_{\beta\alpha}^i - |m_{\alpha\beta}^i|^2 \right).
\end{aligned} \tag{4.12}
$$

Combining the direct part and the exchange part, we obtain

$$
H_U = \frac{U}{2} \sum_i \sum_{\alpha\beta,\alpha\neq\beta} \left[2n_{i\alpha}\hat{n}_{i\beta} - n_{i\alpha}n_{i\beta} - 2m_{\alpha\beta}^i \hat{m}_{\beta\alpha}^i + |m_{\alpha\beta}^i|^2 \right]. \tag{4.13}
$$

In the bulk case, the HF study confirms the all-in/all-out[64] magnetic configuration for $U = 0.7 - 1.8\text{eV}$.

4.7 Self-consistent calculation

For each site, we input 36 randomly generated real numbers as the initial trial of $m_{\alpha\beta}^i$, then the new $m_{\alpha\beta}^i$ is calculated from the contribution of all the occupied states. With around 50 sets of initial inputs, we select the converged result with the minimum total energy. The convergence criterion is

$$|\text{Re}(m_{\alpha\beta}^{i,in} - m_{\alpha\beta}^{i,out})| < 10^{-8},$$
$$|\text{Im}(m_{\alpha\beta}^{i,in} - m_{\alpha\beta}^{i,out})| < 10^{-8}. \tag{4.14}$$

Around two thirds of those calculations converge.

To calculate the local magnetic moments, we first determine the g factor by

$$g\langle \mathbf{j}^2 \rangle = \langle (-g_l \mathbf{l} + g_s \mathbf{s}) \cdot \mathbf{j} \rangle, \tag{4.15}$$

where the total angular momentum $\mathbf{j} = -\mathbf{l} + \mathbf{s}$ is defined in the *local* coordinates of t_{2g}, and $g_l = 1, g_s = 2$. Then the total magnetic moment is calculated

$$\mathbf{m} = g\mu_B \langle \mathbf{j} \rangle. \tag{4.16}$$

The Z_2[92] and Chern numbers[40] are calculated with Fukui's algorithm.

4.8 Phase diagrams and band structures

The phase diagram we obtained is shown in Fig.4.6, and the corresponding band structure is shown in Fig.4.7. The phase diagram has some

important features. In general, it is similar to the $t_s = t$ bilayer case and $t_s = -t$ TKT trilayer case in our previous chapter, but there is also an important difference. The topological insulating states and Chern insulating states are now replaced by corresponding metallic states.
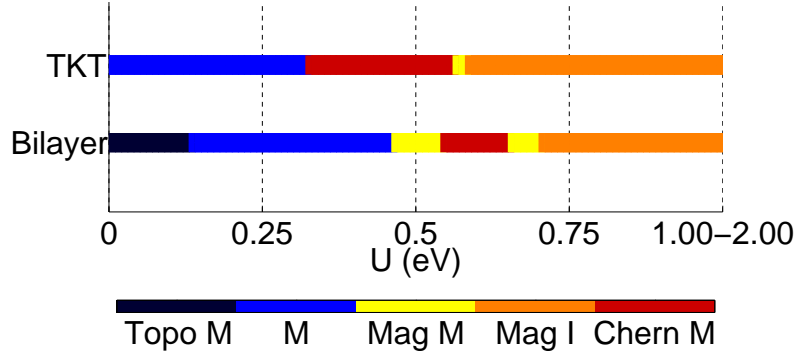
Figure 4.6: Phase diagram of the bilayer and TKT thin films from HF studies. The interaction strength is tuned in the horizontal axis. A Z_2 topological metal phase emerges in bilayer film with time reversal symmetry preserved for small U. Chern metals are predicted in both the bilayer and TKT films centered around $U \approx 0.6$ eV and $U \approx 0.5$ eV respectively. The different phases are abbreviated as: Topo M=topological metal, M=metal, Mag M=magnetic metal, Mag I=magnetic insulator, and Chern M = Chern Metal.

In the bilayer case, for a small U, the system is Z_2 topological metallic[104]. The state reveals a negative indirect gap, but the direct gap is still open. As U is increased, the valence and conduction bands touch each other and separate, turning the metallic state into a trivial one. After the film turns magnetic, it first appears as a metal. In a region around $U = 0.60$eV, the bilayer thin film can still become Chern metallic. As U is increased, the system becomes trivial metallic again, and finally magnetic insulator.
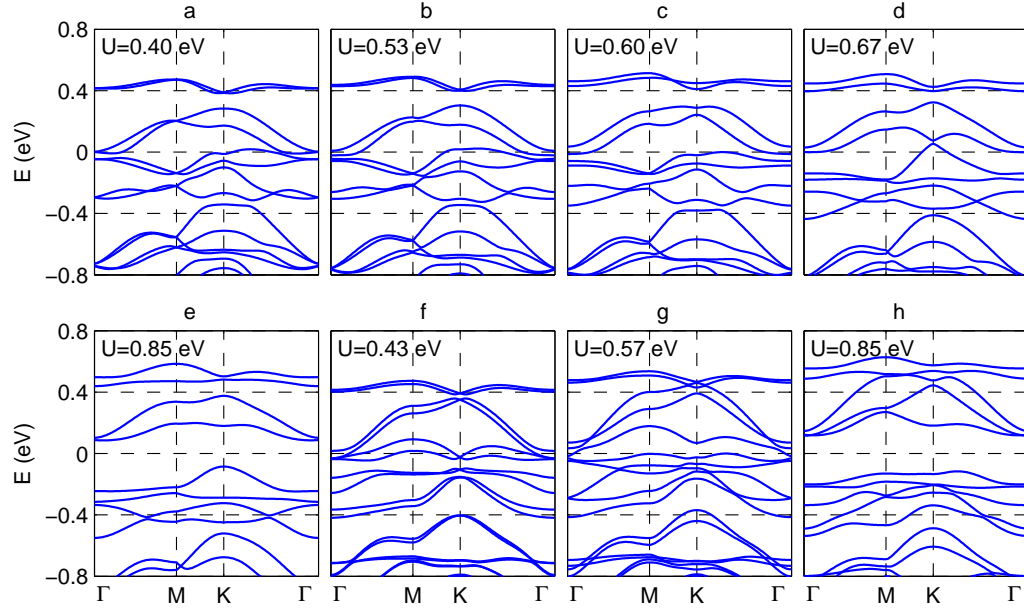
Figure 4.7: The change of electric band structure corresponding to phases in Fig.4.6. The interaction strength is shown on the figure. (a)-(e) The bilayer thin film undergoes phase transitions: M→Mag M→Chern M→Mag M→Mag I. (f)-(h) The TKT thin film undergoes phase transitions: Chern M→Mag M→Mag I. The Fermi surfaces are reset to zero in each figure.

.

In the TKT trilayer case, there exist nearly flat bands close to the Fermi surface. At a large enough U, the nearly flat bands split and the bands under the direct gap possess a Chern number which is equal to ± 1, but the indirect gap is negative. As U is increased, we can see the upper bands will push the conduction band and cause a mixing between them, and extinguish the topological states.

In order to turn those topological metallic states into their insulating counterparts, the possible methods include strain or charge-density waves. The charge-density wave approach is realistic, since the $5d$ orbitals are fairly extended, the nearest neighbor interaction may have an important impact on the band structures.
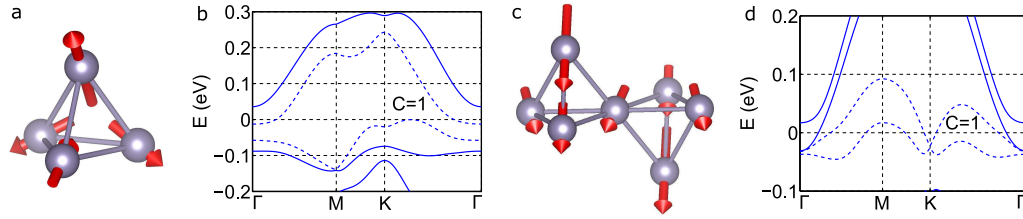
Figure 4.8: The magnetic configurations (a),(c) and electric structure (b),(d) of the Chern metallic phase. (a)-(b) In the bilayer thin film when $U = 0.60$ eV. (c)-(d) In the TKT thin film when $U = 0.43$ eV. In (b) and (d), the dashed lines represent the valence and conduction bands, and $C = 1$ represents the total Chern number of the bands under each direct gap.

To hava a close look at the Chern metallic phase, magnified bandstructure and magnetic profiles are shown in Fig.4.8. At large U, in both the bilayer and trilayer case, the magnetic configurations are fairly stable, and have the patterns shown in Fig.4.9.

65
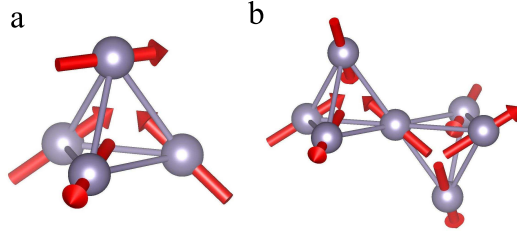
Figure 4.9: The local magnetic moments at large U in bilayer and TKT trilayer thin films. (a) The $U = 1.30$eV case in bilayer thin film. The three ions in the kagome plane possess magnetic moments with the same magnitude. (b) The $U = 1.20$eV case in TKT thin film. The three ions in the kagome plane possess magnetic moments with the same magnitude.

4.9 Comparison between slab-truncation method and superlattice projection

As we pointed out previously, the slab-truncation of the bulk tight-binding model gives a band structure close to the superlattice DFT calculation in the bilayer case, but the deviation is not very small, so it is beneficial to look at the results obtained directly from the superlattice Wannier projection and compare the result with slab truncation.

The superlattice Wannier projection is carried out with a method similar to the bulk Wannier projection. The Monkhorst-Pack grid[98] for it is $9 \times 9 \times 1$. The trial basis functions are selected in a way similar to the bulk case. The projection produces a band structure which is very close to the DFT calculation, as shown in Fig.4.10. Then we use it as a starting point of the HF approximation calculation.

The comparison of the phase diagrams are shown in Fig.4.11. The phase diagrams obtained from the two ways agree qualitatively, although the
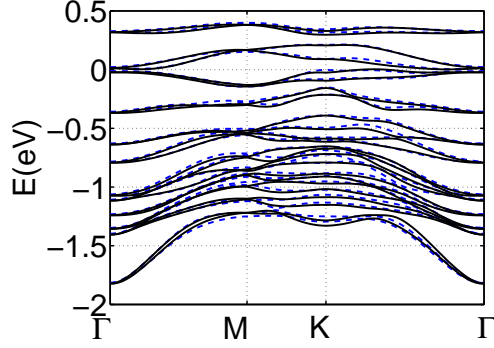
Figure 4.10: Comparison between bands from supercells DFT calculation and superlattice Wannier fit. The DFT results are obtained from a fully relaxed GGA+SOC calculation (solid black). The dashed blue curves are from the tight-binding model obtained from superlattice Wannier projection. Notice that the fitting is much better than Fig.4.5(a).

phase boundaries shift. The region for the Z_2 topological metals shrink a lot, but the region for the Chern metal is enlarged. The comparison verified the effectiveness of the naive slab-truncation method in determining the topological phases.

We also need to point out that the magnetic configurations obtained in those two different ways are different. That is not hard to understand since in the thin films the positions of the iridium ions are already changed with respect to the ideal locations. The equivalence of the magnetic moments for the in-plane ions in the previous calculation (See Fig.4.9) no longer exist in our new calculation with the slab Wannier functions. For example, when $U = 1.00$eV, the three in-plane magnitudes are $0.6502\mu_B$, $1.0176\mu_B$, and $0.6468\mu_B$. In our previous method, when $U = 1.00$eV, those values are all $1.1176\mu_B$.
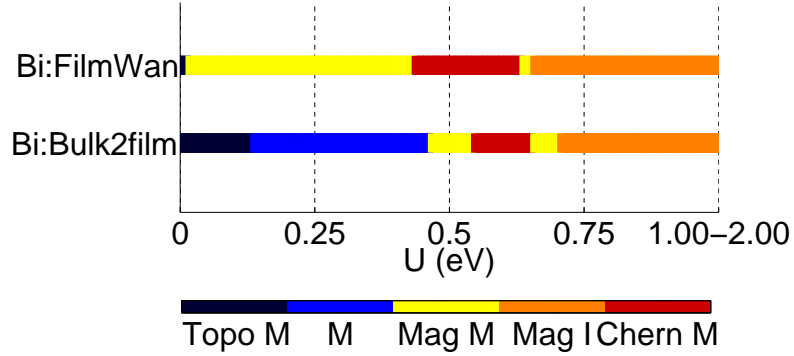
Figure 4.11: Phase diagram of the bilayer thin films with two different ways of constructing the non-interacting Hamiltonian. In the top one, the non-interacting Hamiltonian is obtained from a Wannier fit in the superlattice. In the bottom one, the non-interacting Hamiltonian is obtained from the slab-truncation of the bulk Wannier fit.

4.10   Discussion and Conclusions

In this chapter, we reveal the extended nature of the $5d$ orbitals in iridates. The hopping between iridium ions a few lattice constants away still can still play a role. In order to establish a reasonable tight-binding model, a lot of hopping terms must be included.

Despite the extended nature of $5d$ orbitals, a slab-truncation method to obtain the tight-binding models of thin films still works well in determining the topological states. That is due to the robustness of those states.

Although the topolgical states in real thin films appears metallic, charge-density wave may be a realistic way to convert them into their insulating counterparts. As we mentioned in the previous chapter, the dynamic fluctuation effect may enhance instead of destroying those topological states. A dynamic

mean-field theory calculation with charge-density wave present is still worth-while.

Appendix

Appendix 1

Input file of Wannier90 for bulk $Y_2Ir_2O_7$

For an explanation of this input file, please refer to Chap.4.

num_wann=24

spinors=true

dis_win_min=11.1119

dis_win_max=13.9119

num_bands = 236

num_iter   = 0

Begin Atoms_Cart

Bohr

Y   9.55179600   9.55179600   9.55179600

Y   9.55179600   14.32769400   14.32769400

Y 14.32769400   14.32769400   9.55179600

Y 14.32769400   9.55179600   14.32769400

Ir 0.00000000   0.00000000   0.00000000

Ir 0.00000000   4.77589800   4.77589800

Ir 4.77589800   4.77589800   0.00000000

Ir 4.77589800   0.00000000   4.77589800

O   6.40658061   2.38794900   2.38794900

O 12.69701139   16.71564300   16.71564300

O 16.71564300   11.18247861   7.16384700

O   2.38794900   17.47290939   2.38794900

O 2.38794900   6.40658061   2.38794900

O 16.71564300   12.69701139   16.71564300

O 17.47290939   2.38794900   2.38794900

O 11.18247861   7.16384700   16.71564300

O 7.16384700   16.71564300   11.18247861

O 2.38794900   2.38794900   17.47290939

O 2.38794900   2.38794900   6.40658061

O 16.71564300   16.71564300   12.69701139

O 7.16384700   7.16384700   7.16384700

O 11.93974500   11.93974500   11.93974500

End Atoms_Cart

Begin Projections

! Ir1

 f=0, 0, 0 : l=2, mr=3 : z=-2, -2, 1 : x=2, -1, 2 : zona=0.5

 f=0, 0, 0 : l=2, mr=2 : z=-2, -2, 1 : x=2, -1, 2 : zona=0.5

 f=0, 0, 0 : l=2, mr=5 : z=-2, -2, 1 : x=2, -1, 2 : zona=0.5

! Ir2

 f=0.5, 0, 0 : l=2, mr=3 : z=1, 2, 2 : x=2, -2, 1 : zona=0.5

 f=0.5, 0, 0 : l=2, mr=2 : z=1, 2, 2 : x=2, -2, 1 : zona=0.5

 f=0.5, 0, 0 : l=2, mr=5 : z=1, 2, 2 : x=2, -2, 1 : zona=0.5

! Ir3

 f=0, 0.5, 0 : l=2, mr=3 : z=2, 1, 2 : x=1, 2, -2 : zona=0.5

 f=0, 0.5, 0 : l=2, mr=2 : z=2, 1, 2 : x=1, 2, -2 : zona=0.5

 f=0, 0.5, 0 : l=2, mr=5 : z=2, 1, 2 : x=1, 2, -2 : zona=0.5

73

! Ir4

 f=0, 0, 0.5 : l=2, mr=3 : z=2,-1,-2 : x=1, -2, 2 : zona=0.5

 f=0, 0, 0.5 : l=2, mr=2 : z=2,-1,-2 : x=1, -2, 2 : zona=0.5

 f=0, 0, 0.5 : l=2, mr=5 : z=2,-1,-2 : x=1, -2, 2 : zona=0.5

End Projections

bands_plot = true

bands_plot_format = gnuplot

wannier_plot_supercell=3

hr_plot= true

begin kpoint_path

 X 0.000 0.500 0.500   W 0.250 0.500 0.750

 W 0.250 0.500 0.750   G 0.000 0.000 0.000

 G 0.000 0.000 0.000   L 0.500 0.000 0.000

 L 0.500 0.500 0.500   K 0.375 0.375 0.750

 K 0.375 0.375 0.750   X 0.000 0.500 0.500

end kpoint_path

Begin Unit_Cell_Cart

Bohr

 0.00000000 9.55179600 9.55179600

 9.55179600 0.00000000 9.55179600

 9.55179600 9.55179600 0.00000000

74

End Unit_Cell_Cart

mp_grid   = 8 8 8

begin kpoints

  (This part is omitted)

end kpoints

Bibliography

[1] E. H. Hall, American Journal of Mathematics **2**, 287 (1879).

[2] K. v. Klitzing, G. Dorda, and M. Pepper, Phys. Rev. Lett. **45**, 494 (1980).

[3] H. L. Stormer and D. C. Tsui, Science **220**, 1241 (1983).

[4] D. J. Thouless, M. Kohmoto, M. P. Nightingale, and M. den Nijs, Phys. Rev. Lett. **49**, 405 (1982).

[5] F. D. M. Haldane, Phys. Rev. Lett. **61**, 2015 (1988).

[6] K. Novoselov, A. K. Geim, S. Morozov, D. Jiang, M. Katsnelson, I. Grigorieva, S. Dubonos, and A. Firsov, Nature **438**, 197 (2005).

[7] C. L. Kane and E. J. Mele, Phys. Rev. Lett. **95**, 146802 (2005).

[8] C. L. Kane and E. J. Mele, Phys. Rev. Lett. **95**, 226801 (2005).

[9] M. König, S. Wiedmann, C. Brune, A. Roth, H. Buhmann, L. Molenkamp, X.-L. Qi, and S.-C. Zhang, Science **318**, 766 (2007).

[10] A. Roth, C. Brüne, H. Buhmann, L. W. Molenkamp, J. Maciejko, X.-L. Qi, and S.-C. Zhang, Science **325**, 294 (2009).

[11] D. Hsieh, D. Qian, L. Wray, Y. Xia, Y. Hor, R. J. Cava, and M. Z. Hasan, Nature **452**, 970 (2008).

[12] D. Hsieh, Y. Xia, L. Wray, D. Qian, A. Pal, J. H. Dil, J. Osterwalder, F. Meier, B. Bihlmayer, C. L. Kane, Y. Hor, R. J. Cava, and M. Z. Hasan, Science **323**, 919 (2009).

[13] Y. Xia, D. Qian, D. Hsieh, L. Wray, A. Pal, H. Lin, A. Bansil, D. Grauer, Y. S. Hor, R. J. Cava, and M. Z. Hasan, Nature Phys. **5**, 398 (2009).

[14] H. Zhang, C.-X. Liu, X.-L. Qi, X. Dai, Z. Fang, and S.-C. Zhang, Nature Phys. **5**, 438 (2009).

[15] S. Chadov, X.-L. Qi, J. Kübler, G. H. Fecher, C. Felser, and S.-C. Zhang, Nat. Mat. **9**, 541 (2010).

[16] J. Wang, R. Li, S.-C. Zhang, and X.-L. Qi, Phys. Rev. Lett. **106**, 126403 (2011).

[17] W. Feng, D. Xiao, J. Ding, and Y. Yao, Phys. Rev. Lett. **106**, 016402 (2011).

[18] H.-J. Zhang, S. Chadov, L. Müchler, B. Yan, X.-L. Qi, J. Kübler, S.-C. Zhang, and C. Felser, Phys. Rev. Lett. **106**, 156402 (2011).

[19] D. Xiao, Y. Yao, W. Feng, J. Wen, W. Zhu, X.-Q. Chen, G. M. Stocks, and Z. Zhang, Phys. Rev. Lett. **105**, 096404 (2010).

[20] H. Lin, R. S. Markiewicz, L. A. Wray, L. Fu, M. Z. Hasan, and A. Bansil, Phys. Rev. Lett. **105**, 036404 (2010).

[21] Y. L. Chen, Z. K. Liu, J. G. Analytis, J.-H. Chu, H. J. Zhang, B. H. Yan, S.-K. Mo, R. G. Moore, D. H. Lu, I. R. Fisher, S. C. Zhang, Z. Hussain, and Z.-X. Shen, Phys. Rev. Lett. **105**, 266401 (2010).

[22] B. Yan, C.-X. Liu, H.-J. Zhang, C.-Y. Yam, X.-L. Qi, T. Frauenheim, and S.-C. Zhang, Europhys. Lett. **90**, 37002 (2010).

[23] B. Yan, H.-J. Zhang, C.-X. Liu, X.-L. Qi, T. Frauenheim, and S.-C. Zhang, Phys. Rev. B **82**, 161108 (2010).

[24] R. Yu, W. Zhang, H.-J. Zhang, S.-C. Zhang, X. Dai, and Z. Fang, Science **329**, 61 (2010).

[25] C.-Z. Chang, J. Zhang, X. Feng, J. Shen, Z. Zhang, M. Guo, K. Li, Y. Ou, P. Wei, L.-L. Wang, Z.-Q. Ji, Y. Feng, Shuaihua, X. Chen, J. Jia, X. Dai, Z. Fang, S.-C. Zhang, K. He, Y. Wang, L. Lu, X.-C. Ma, and Q.-K. Xue, Science **340**, 167 (2013).

[26] W. Kohn and L. J. Sham, Phys. Rev. **140**, A1133 (1965).

[27] P. Hohenberg and W. Kohn, Phys. Rev. **136**, B864 (1964).

[28] N. Marzari, A. A. Mostofi, J. R. Yates, I. Souza, and D. Vanderbilt, Rev. Mod. Phys. **84**, 1419 (2012).

[29] D. N. Sheng, Z.-C. Gu, K. Sun, and L. Sheng, Nat. Commun. **2**, 389 (2011).

[30] K. Sun, Z. Gu, H. Katsura, and S. Das Sarma, Phys. Rev. Lett. **106**, 236803 (2011).

[31] T. Neupert, L. Santos, C. Chamon, and C. Mudry, Phys. Rev. Lett. **106**, 236804 (2011).

[32] E. Tang, J.-W. Mei, and X.-G. Wen, Phys. Rev. Lett. **106**, 236802 (2011).

[33] Y.-F. Wang, Z.-C. Gu, C.-D. Gong, and D. N. Sheng, Phys. Rev. Lett. **107**, 146803 (2011).

[34] A. Shimoyamada, S. Tsuda, K. Ishizaka, T. Kiss, T. Shimojima, T. Togashi, S. Watanabe, C. Q. Zhang, C. T. Chen, Y. Matsushita, H. Ueda, Y. Ueda, and S. Shin, Phys. Rev. Lett. **96**, 026403 (2006).

[35] A. Rüegg and G. A. Fiete, Phys. Rev. B **84**, 201103 (2011).

[36] K.-Y. Yang, W. Zhu, D. Xiao, S. Okamoto, Z. Wang, and Y. Ran, Phys. Rev. B **84**, 201104 (2011).

[37] K. Osterloh, M. Baig, L. Santos, P. Zoller, and M. Lewenstein, Phys. Rev. Lett. **95**, 010403 (2005).

[38] Y.-J. Lin, R. L. Compton, A. R. Perry, W. D. Phillips, J. V. Porto, and I. B. Spielman, Phys. Rev. Lett. **102**, 130401 (2009).

[39] I. B. Spielman, Phys. Rev. A **79**, 063613 (2009).

[40] T. Fukui, Y. Hatsugai, and H. Suzuki, J. Phys. Soc. Jap. **74**, 1674 (2005).

[41] For a description of the differential evolution method see: http://www.nehu-economics.info/difevol.html.

[42] L. Fu and C. L. Kane, Phys. Rev. B **76**, 045302 (2007).

[43] S. Raghu, X.-L. Qi, C. Honerkamp, and S.-C. Zhang, Phys. Rev. Lett. **100**, 156401 (2008).

[44] K. Sun, H. Yao, E. Fradkin, and S. A. Kivelson, Phys. Rev. Lett. **103**, 046811 (2009).

[45] J. Wen, A. Rüegg, C.-C. J. Wang, and G. A. Fiete, Phys. Rev. B **82**, 075125 (2010).

[46] Y. Zhang, Y. Ran, and A. Vishwanath, Phys. Rev. B **79**, 245331 (2009).

[47] Q. Liu, H. Yao, and T. Ma, Phys. Rev. B **82**, 045102 (2010).

[48] A. S. Sørensen, E. Demler, and M. D. Lukin, Phys. Rev. Lett. **94**, 086803 (2005).

[49] M. Hafezi, A. S. Sørensen, E. Demler, and M. D. Lukin, Phys. Rev. A **76**, 023613 (2007).

[50] L.-M. Duan, E. Demler, and M. D. Lukin, Phys. Rev. Lett. **91**, 090402 (2003).

[51] J. Ruostekoski, Phys. Rev. Lett. **103**, 080406 (2009).

[52] D. Bercioux, D. F. Urban, H. Grabert, and W. Häusler, Phys. Rev. A **80**, 063603 (2009).

[53] D. Bercioux, N. Goldman, and D. F. Urban, Phys. Rev. A **83**, 023609 (2011).

[54] N. Goldman, D. F. Urban, and D. Bercioux, Phys. Rev. A **83**, 063601 (2011).

[55] X. Hu, M. Kargarian, and G. A. Fiete, Phys. Rev. B **84**, 155116 (2011).

[56] Y. Ando, J. Phys. Soc. Jpn. **82**, 102001 (2013).

[57] D.-X. Qu, Y. S. Hor, J. Xiong, R. J. Cava, and N. P. Ong, Science **329**, 821 (2010).

[58] W. Witczak-Krempa, G. Chen, Y. B. Kim, and L. Balents, Ann. Rev. Cond. Matt. Phys. **5**, 57 (2014).

[59] D. Pesin and L. Balents, Nature Phys. **6**, 376 (2010).

[60] M. Kargarian, J. Wen, and G. A. Fiete, Phys. Rev. B **83**, 165112 (2011).

[61] M. Kargarian and G. A. Fiete, Phys. Rev. Lett. **110**, 156403 (2013).

[62] J. Maciejko, V. Chua, and G. A. Fiete, Phys. Rev. Lett. **112**, 016404 (2014).

[63] A. Go, W. Witczak-Krempa, G. S. Jeon, K. Park, and Y. B. Kim, Phys. Rev. Lett. **109**, 066401 (2012).

[64] X. Wan, A. M. Turner, A. Vishwanath, and S. Y. Savrasov, Phys. Rev. B **83**, 205101 (2011).

[65] Y. Wang, Z. Wang, Z. Fang, and X. Dai, Phys. Rev. B **91**, 125139 (2015).

[66] W. Witczak-Krempa and Y. B. Kim, Phys. Rev. B **85**, 045124 (2012).

[67] A. Rüegg, C. Mitra, A. A. Demkov, and G. A. Fiete, Phys. Rev. B **85**, 245131 (2012).

[68] D. Xiao, W. Zhu, Y. Ran, N. Nagaosa, and S. Okamoto, Nat. Comm. **2**, 596 (2011).

[69] S. Okamoto, W. Zhu, Y. Nomura, R. Arita, D. Xiao, and N. Nagaosa, Phys. Rev. B **89**, 195121 (2014).

[70] B.-J. Yang and N. Nagaosa, Phys. Rev. Lett. **112**, 246402 (2014).

[71] S. Okamoto, Phys. Rev. Lett. **110**, 066403 (2013).

[72] D. Doennig, W. E. Pickett, and R. Pentcheva, Phys. Rev. B **89**, 121110 (2014).

[73] J. L. Lado, V. Pardo, and D. Baldomir, Phys. Rev. B **88**, 155119 (2013).

[74] Q.-F. Liang, L.-H. Wu, and X. Hu, New J. Phys. **15**, 063031 (2013).

[75] X. Hu, A. Rüegg, and G. A. Fiete, Phys. Rev. B **86**, 235141 (2012).

[76] F. Wang and Y. Ran, Phys. Rev. B **84**, 241103 (2011).

[77] J. Mannhart and D. Schlom, Science **327**, 1607 (2010).

[78] J. Mannhart, D. Blank, H. Hwang, A. Millis, and J.-M. Triscone, Mat. Res. Bull **33**, 1027 (2008).

[79] P. Zubko, S. Gariglio, M. Gabay, P. Ghosez, and J.-M. Triscone, Ann. Rev. Cond. Matt. Phys. **2**, 141 (2011).

[80] A. V. Boris, Y. Matiks, E. Benckiser, A. Frano, P. Popovich, V. Hinkov, P. Wochner, M. Castro-Colin, E. Detemple, V. K. Malik, C. Bernhard, T. Prokscha, A. Suter, Z. Salman, E. Morenzoni, G. Cristiani, H.-U. Habermeier, and B. Keimer, Science **332**, 937 (2011).

[81] E. Benckiser, M. W. Haverkort, S. Brack, E. Goering, S. Macke, A. Frañó, X. Yang, O. K. Andersen, G. Cristiani, H.-U. Habermeier, A. V. Boris, I. Zegkinoglou, P. Wochner, H.-J. Kim, V. Hinkov, and B. Keimer, Nature Mater. **10**, 189 (2011).

[82] J. Chakhalian, J. M. Rondinelli, J. Liu, B. A. Gray, M. Kareev, E. J. Moon, N. Prasai, J. L. Cohn, M. Varela, I. C. Tung, M. J. Bedzyk, S. G.

Altendorf, F. Strigari, B. Dabrowski, L. H. Tjeng, P. J. Ryan, and J. W. Freeland, Phys. Rev. Lett. **107**, 116805 (2011).

[83] J. Liu, S. Okamoto, M. van Veenendaal, M. Kareev, B. Gray, P. Ryan, J. W. Freeland, and J. Chakhalian, Phys. Rev. B **83**, 161102 (2011).

[84] J. Son, P. Moetakef, J. LeBeau, D. Ouellette, L. Balents, S. Allen, and S. Stemmer, Appl. Phys. Lett. **96**, 062114 (2010).

[85] J. Son, P. Moetakef, J. LeBeau, and S. Stemmer, Appl. Phys. Lett. **97**, 202109 (2010).

[86] M. Gibert, P. Zubko, R. Scherwitzl, J. Iniguez, and J.-M. Triscone, Nat Mater **11**, 195 (2012).

[87] G. Herranz, F. Sanchez, N. Dix, M. Scigaj, and J. Fontcuberta, Sci. Rep. **2**, 758 (2012).

[88] S. Middey, D. Meyers, M. Kareev, E. J. Moon, B. A. Gray, X. Liu, J. W. Freeland, and J. Chakhalian, Appl. Phys. Lett. **101**, 261602 (2012).

[89] S. Maekawa, T. Tohyama, S. E. Barnes, S. Ishihara, W. Koshinbae, and G. Khaliullin, *Physics of Transition Metal Oxides* (Springer, Berlin, 2004).

[90] B.-J. Yang and Y. B. Kim, Phys. Rev. B **82**, 085111 (2010).

[91] J. C. Slater and G. F. Koster, Phys. Rev. **94**, 1498 (1954).

84

[92] T. Fukui and Y. Hatsugai, J. Phys. Soc. Jap. **76**, 053702 (2007).

[93] Q. Chen, H.-H. Hung, X. Hu, and G. A. Fiete, arXiv preprint arXiv:1504.03646 (2015).

[94] X. Hu, Z. Zhong, and G. A. Fiete, Sci. Rep. **5**, 11072 (2015).

[95] N. Taira, M. Wakeshima, and Y. Hinatsu, J. Phys.: Condens. Matter **13**, 5527 (2001).

[96] P. Blaha, K. Schwarz, G. K. H. Madsen, D. Kvasnicka, and J. Luitz, *WIEN2K, An Augmented Plane Wave + Local Orbitals Program for Calculating Crystal Properties* (Karlheinz Schwarz, Techn. Universität Wien, Austria, 2001).

[97] P. Giannozzi, S. Baroni, N. Bonini, *et al.*, J. Phys.: Condens. Matter **21**, 395502 (2009).

[98] H. J. Monkhorst and J. D. Pack, Phys. Rev. B **13**, 5188 (1976).

[99] A. Rüegg, C. Mitra, A. A. Demkov, and G. A. Fiete, Phys. Rev. B **88**, 115146 (2013).

[100] A. A. Mostofi, J. R. Yates, Y.-S. Lee, I. Souza, D. Vanderbilt, and N. Marzari, Comput. Phys. Commun. **178**, 685 (2008).

[101] J. Rieken, I. Anderson, and M. Kramer, *Innovative Powder Processing of Oxide Dispersion Strengthened ODS Ferritic Stainless Steels*, Tech. Rep. (Ames Laboratory (AMES), Ames, IA (United States), 2011).

[102] T. Takeda, Z. Phys. B Con. Mat. **32**, 43 (1978).

[103] H. Zhang, K. Haule, and D. Vanderbilt, Phys. Rev. Lett. **111**, 246402 (2013).

[104] M. Z. Hasan and C. L. Kane, Rev. Mod. Phys. **82**, 3045 (2010).

Vita

Xiang Hu was born in Changde, Hunan province, China. He received the Bachelor of Engineering degree from Zhengzhou University in 2002, and the Master of Science degree in Physics from Peking University in 2005. In August 2006, he joined the Graduate School at University of Houston. He received the Master of Science degree in Physics from University of Houston in 2008. He left University of Houston in July 2009, and entered the Graduate School at the University of Texas at Austin in August 2009, to pursue a PhD in Physics.

Permanent address: 3363 Lake Austin Blvd, Apt B
Austin, Texas 78703

This dissertation was typed by the author.